

Level 2 Photometric Calibration for the LSST Survey

Lynne Jones, Željko Ivezić, David Burke, Tim Axelrod on behalf of The Photometric Calibration Team

ABSTRACT

This document describes the photometric calibration procedure for LSST Data Release catalogs. This procedure will use specialized hardware (an auxiliary telescope and narrow-band dome screen projector) to measure the wavelength dependence of the atmospheric and hardware response functions, together with a self-calibration procedure that leverages multiple observations of the same sources over many epochs, to deliver 1%-level photometry across the observed sky.

1. Introduction

LSST aims to deliver 1%-level photometry across the observed sky (0.5%-level for repeat observations of the same source), representing about a factor of two improvement over the current state-of-the-art wide-field optical photometry delivered by SDSS. This factor of two improvement will have a major impact on science deliverables because it implies that the error volume in the five-dimensional LSST color space will be almost two orders of magnitude smaller than for SDSS-like photometry. This smaller error volume will improve source classification and the precision of quantities such as photometric redshifts for galaxies and photometric metallicity for stars.

This factor of two improvement results from two major differences between LSST and SDSS. First, each source will receive hundreds of observations over the ten years of the LSST survey. These series of repeat observations will be used to self-calibrate the photometric system across the sky and for each observation (akin, but not identical to, the uber-calibration procedure used by SDSS (Padmanabhan et al. 2008)), allowing LSST to operate in a wide variety of conditions. Secondly, the wavelength dependence of the hardware and atmospheric transmission response functions will be measured with auxiliary instrumentation on sufficiently fine angular and temporal scales to enable their explicit inclusion in the calibration procedure, rather than resorting to traditional approximations such as linear color terms. CFHT Legacy Survey listed these wavelength-dependent effects as their primary remaining source of error (Regnault et al. 2009).

This document describes the calibration requirements and processes for LSST Data Release photometry. This is a complete recalibration of the data carried out at periodic Data

Release dates, approximately annually (aka Level 2 Data products, in LSST Data Management terms). There will also be a real-time data calibration process, based on the best available set of prior calibrated observations, to provide best-effort precision and accuracy for photometry for quality assurance, generation of alerts, and other quantities appropriate for nightly data generation (aka Level 1 Data Product). The Level 1 photometric calibration is not discussed here.

Section 2 reviews the survey requirements for photometric calibration, while Section 3 describes the philosophy behind LSST’s calibration procedure, first motivating this procedure by describing the true path of a photon through the atmosphere and LSST system and then from the calibration point of view, trying to recreate the transmission of those photons to the focal plane. Section 4 describes details of each step of the calibration procedure, including how each calibration measurement is obtained and applied to the science data along with expected errors originating from each step.

2. Photometric Requirements

The LSST Science Requirements Document (SRD) provides a set of requirements on the annual Data Release (Level 2) photometry based on measurements of bright, unresolved, isolated, non-variable objects from individual LSST visits. Bright implies that the measurement of the star’s brightness is not dominated by photon statistics, approximately 1-4 magnitudes fainter than the saturation limit in a given filter. Isolated implies that the star does not have de-blending problems with background galaxies or nearby stars. Non-variable objects are intrinsically not variable; these will be identified in an iterative fashion from the many epochs of LSST observations. The SRD specifications are:

1. **Repeatability:** the median value of the rms of calibrated magnitude measurements around the mean calibrated magnitude for each star will not exceed 5 millimags in *gri*, 7.5 millimags in *uzy* for bright, unresolved, isolated, non-variable objects. No more than 10% of these objects should have an rms larger than 15 mmag in *gri*, 22.5 mmag in *uzy*. This specifies the distribution of random photometric errors (σ) and constrains both the repeatability of extracting counts from images and the ability to monitor (or model) the changes in normalized system response (ϕ). It could be thought of as making the photometry of a single source consistent over time.
2. **Uniformity:** the rms of the internal photometric zeropoint error (for each visit) will not exceed 10 millimags in *grizy*, 20 millimags in *uzy*, where the zeropoint for each visit is determined using bright, unresolved, isolated, non-variable sources. No more than

10% of these sources should be more than 15 mmag in *gri* or 22.5 mmag in *uzy* from the mean internal zeropoint. This places a constraint on the stability of the photometric system across the sky as well as places an upper limit on various systematic errors, such as any correlation of photometric calibration with varying stellar populations (or colors). This makes the photometry of many sources comparable over the entire sky, which when combined with the previous requirements creates a stable photometric system across the sky and over time, in a single filter.

3. **Band-to-band photometric calibration:** The absolute band-to-band zeropoint calibration for main sequence stars must be known with an rms accuracy of 5 millimags for any color not involving *u* band, 10 millimags for colors constructed with *u* band photometry. This places an upper limit on the systematic error in the measurement of the system throughput as a function of wavelength. This requirement ties photometric measurements in different filters together, enabling colors to be measured for sources with unknown spectral energy distributions (SEDs) or (for sources with known SEDs) magnitudes in different filters to be directly compared.
4. **Absolute photometric calibration:** The LSST photometric system must transform to an external physical scale (*e.g.* AB mags) with an rms accuracy of 10 millimags. This requirement ties LSST internal photometry to a physical scale, and places a constraint on the upper limit of the systematic error in the measurement of the total system throughput. This final step enables LSST photometry to be compared with photometry from other telescopes using other photometric systems.

Requirements 1 and 2 must be met by measuring and then correcting for changes in hardware and atmospheric transmission as a function of time, location in the sky or focal plane, and result in a relative calibration within a single filter. Requirements 3 and 4 require additional measurements of sources with known colors and absolute magnitudes, providing a relative calibration from filter to filter as well as an absolute physical scale for the overall system.

3. Overview of the photometric calibration process

In traditional photometric calibration, a set of standard stars are observed at a range of airmasses to calculate zeropoint offsets and (typically) a single color-dependent extinction term per night. This is sufficient for photometry at the few percent level on photometric nights, however, historical weather data from Cerro Pachon tells us only 53% of the available observing time can be considered photometric even at the 1–2% level. To take advantage

of the full 85% of the available observing time which is usable (total cloud extinction less than 1.5 magnitudes), and to reach the SRD specified requirements – 0.5% level photometric repeatability and 1% photometric uniformity – requires a new approach.

This new approach lies in splitting the measurement of the *normalization* of the throughput in each observation (the gray-scale zeropoint) from the *shape* of the throughput curve (the color dependent terms), and further, using separate procedures to measure the contributions of the telescope hardware response (to the total normalization and bandpass shape) and the atmospheric throughput (to normalization and shape). This allows the use of optimized methods to measure each individual component affecting the final measured magnitudes, allowing us to achieve photometric calibration at the required levels.

A flowchart showing an overview of the steps from science observation to calibrated photometric measurements, together with the required calibration data products is shown in Figure 1. The *normalization* of the throughput will be corrected by using a flat field (for small spatial scale variations) and the self-calibration procedure (for larger spatial scale variations, as this is fundamentally limited by the spacing between calibration stars in each visit). The flat field can only correct for variations in the throughput of the hardware; the self-calibration procedure will primarily correct for variations in throughput due to atmospheric conditions (such as cloud extinction). The *shape* of the throughput curve will be measured using both the narrow band dome screen projector, to correct for variations in the shape of the hardware bandpass response across the field of view, and the auxiliary telescope, to correct for variations in the atmospheric absorption curve from visit to visit.

The rest of this section will provide a more in-depth overview of the calibration measurements required. We will start with a review of what is physically happening to photons in their path toward the focal plane (the ‘truth’), and then outline how LSST will translate the measured ADU counts back to photons above the atmosphere (the calibration ‘model’).

3.1. Truth: From photons to counts

Let us first consider how the photons from an astronomical object are converted into ADUs in the detector, paying attention to the various temporal or spatial scales for variability might arise in the LSST system to affect the final ADU counts (and ignoring errors in measurement, as this is the ‘truth’ of the flux transmission). This section is intended to motivate the separate measurement of the normalization and shape of the bandpass and introduce some important concepts, such as the normalized system response.

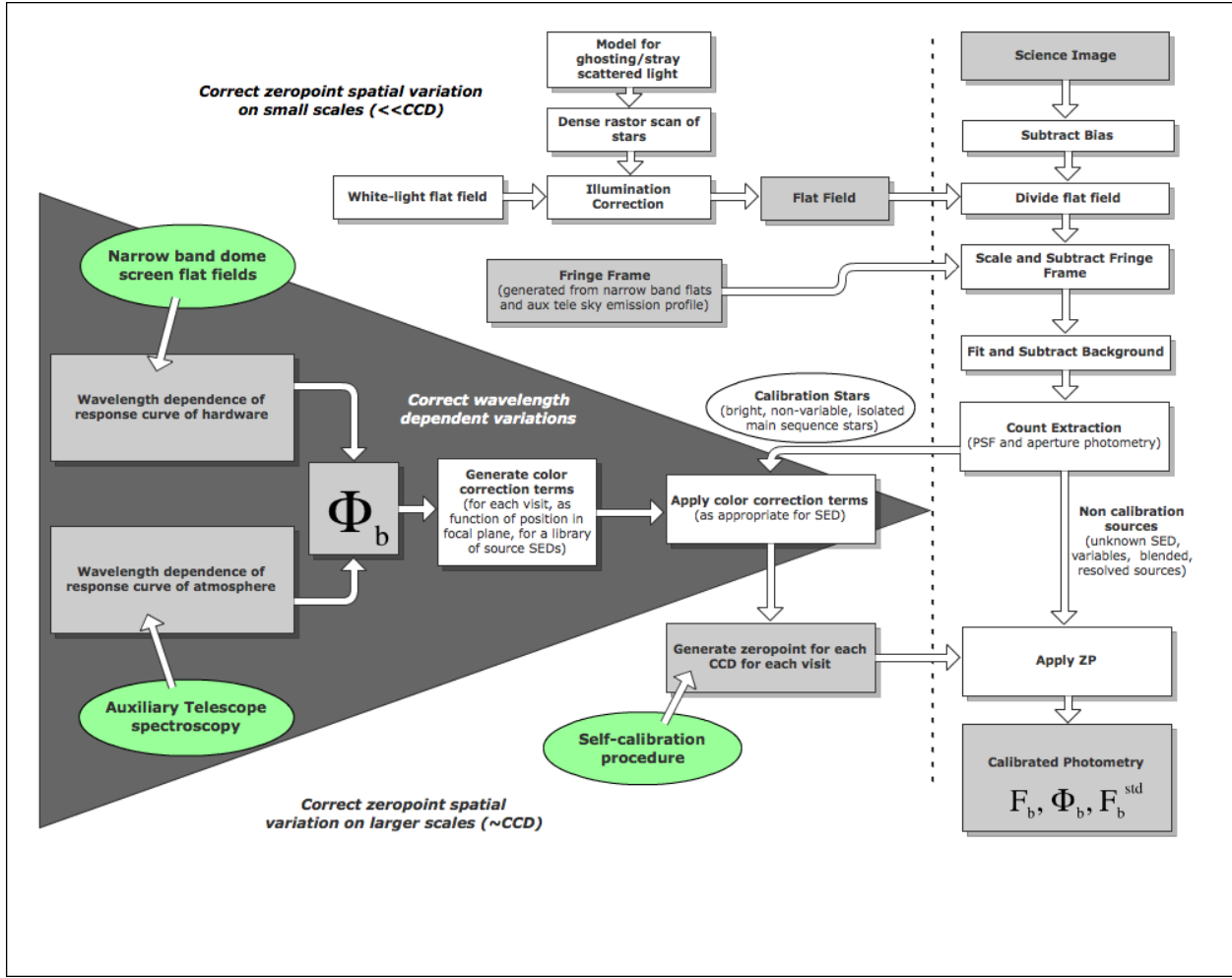


Fig. 1.—: A flowchart of the Data Release photometric calibration process. Everything to the left of the dashed line could be thought of as a calibration product, to be applied to data from each visit on the right of the dashed line. Each of the darker gray boxes indicates data or calibration products required to reach the final goal: calibrated photometric measurements. The light green circles point out significant LSST-specific calibration systems. The separation of the measurement and correction for wavelength dependent (shape) and wavelength independent (normalization) variations in the throughput can be seen in the three sections of the ‘calibration products’ on the left hand side. The upper portion, consisting mainly of flat-field effects, corrects primarily for small spatial scale gray-scale variations (although the illumination correction can have larger spatial scale structure), the middle portion in the dark triangle corrects only for bandpass shape variations, while the bottom portion, consisting of the zeropoint corrections calculated from the self-calibration procedure, will only correct for larger spatial scale variations.

Given $F_\nu(\lambda, t)$ ¹ the specific flux of an astronomical object at the top of the atmosphere, at a position described by (alt, az) , the total flux from the object transmitted through the atmosphere to the telescope pupil is

$$F_\nu^{pupil}(\lambda, alt, az, t) = F_\nu(\lambda, t) S^{atm}(\lambda, alt, az, t), \quad (1)$$

where $S^{atm}(\lambda, alt, az)$ is the (dimensionless) probability that a photon of wavelength λ makes it through the atmosphere,

$$S^{atm}(\lambda, alt, az, t) = e^{-\tau^{atm}(\lambda, alt, az, t)}. \quad (2)$$

Here $\tau^{atm}(\lambda, alt, az)$ is the optical depth of the atmospheric layer at wavelength λ towards the position (alt, az) . Observational data (Stubbs et al. 2007b; Burke et al. 2010) show that the various atmospheric components which contribute to absorption (water vapor, aerosol scattering, Rayleigh scattering and molecular absorption) can lead to variations in $S^{atm}(\lambda, t)$ on the order of 10% per hour. Clouds represent an additional gray (non-wavelength dependent) contribution to τ^{atm} that can vary even more rapidly, on the order of 2–10% of the total extinction at 1° scales within minutes (Ivezić et al. 2007).

Given the above $F_\nu^{pupil}(\lambda, alt, az, t)$, the total ADU counts transmitted from the object to a footprint within the field of view at (x, y) can be written as

$$C_b(alt, az, x, y, t) = C \int_0^\infty F_\nu^{pupil}(\lambda, alt, az, t) S_b^{sys}(\lambda, x, y, t) \lambda^{-1} d\lambda. \quad (3)$$

Here, $S_b^{sys}(\lambda, x, y, t)$ is the (dimensionless) probability that a photon will pass through the telescope’s optical path to be converted into an ADU count, and includes the mirror reflectivity, lens transmission, filter transmision, and detector sensitivity. The term λ^{-1} comes from the conversion of energy per unit frequency into the number of photons per unit wavelength and b refers to a particular filter, *ugrizy*. The dimensional conversion constant C is

$$C = \frac{\pi D^2 \Delta t}{4gh} \quad (4)$$

where D is the effective primary mirror diameter, Δt is the exposure time, g is the gain of the readout electronics (number of photoelectrons per ADU count, a number greater than one),

¹Hereafter, the units for specific flux are Jansky ($1 \text{ Jy} = 10^{-23} \text{ erg cm}^{-2} \text{ s}^{-1} \text{ Hz}^{-1}$). The choice of F_ν vs. F_λ makes the flux conversion to the AB magnitude scale more transparent, and the choice of λ as the running variable is more convenient than the choice of ν . Note also, while $F_\nu(\lambda, t)$ (and other quantities that are functions of time) could vary more quickly than the standard LSST exposure time of 15s, it is assumed that all such quantities are averaged over that short exposure time, so that t refers to quantities that can vary from exposure to exposure.

and h is the Planck constant. The wavelength-dependent variations in S_b^{sys} generally change quite slowly in time; over periods of months, the mirror reflectance and filter transmission will degrade as their coatings age. A more rapidly time-varying wavelength-dependent change in detector sensitivity (particularly at very red wavelengths in the y band) results from temperature changes in the detector, but only on scales equivalent to a CCD or larger. There will also be wavelength-dependent spatial variations in S_b^{sys} due to irregularities in the filter material; these are expected to vary slowly from the center of the field of view to the outer edges, equivalent to a bandpass shift on the order of 1-2% of the effective wavelength of the filter. Wavelength-independent (gray-scale) variations in S_b^{sys} can occur more rapidly, on timescales of a day for variations caused by dust particles on the filter or dewar window, and on spatial scales ranging from the amplifier level, arising from gain changes between amplifiers, down to the pixel level, in the case of pixel-to-pixel detector sensitivity variations.

From equation 3 and the paragraphs above, we can see that the generation of counts $C_b(alt, az, x, y, t)$ from photons is imprinted with many different effects, each with different variability scales over time, space, and wavelength. In particular the wavelength-dependent variability (bandpass shape) is typically much slower in time and space than the gray-scale variations (bandpass normalization). These different scales of variability motivate us to separate the measurement of the normalization of S_b^{sys} and S^{atm} from the measurement of the wavelength-dependent shape of the bandpass.

3.1.1. Normalized bandpass response

This then leads us to introduce a ‘normalized bandpass response function’, $\phi_b^{obs}(\lambda, t)$, for each observation

$$\phi_b^{obs}(\lambda, t) = \frac{S^{atm}(\lambda, alt, az, t) S_b^{sys}(\lambda, x, y, t) \lambda^{-1}}{\int_0^\infty S^{atm}(\lambda, alt, az, t) S_b^{sys}(\lambda, x, y, t) \lambda^{-1} d\lambda}. \quad (5)$$

Note that ϕ_b only represents *shape* information about the bandpass, as by definition, $\int_0^\infty \phi_b(\lambda) d\lambda = 1$.

Using $\phi_b^{obs}(\lambda, t)$ we can represent the above-the-atmosphere specific flux of an object as

$$F_b(t) = \int_0^\infty F_\nu(\lambda) \phi_b^{obs} d\lambda \quad (6)$$

From Equations 1 and 3, we can then recast the counts received from an object as

$$C_b(alt, az, x, y, t) = C \int_0^\infty F_\nu(\lambda, t) S^{atm}(\lambda, alt, az, t) S_b^{sys}(\lambda, x, y, t) \lambda^{-1} d\lambda$$

$$= C'^{atm}(alt, az, t) C_b'^{sys}(x, y, t) \int_0^\infty F_\nu(\lambda, t) \phi_b(\lambda, alt, az, x, y, t) d\lambda \quad (7)$$

where $C'^{atm}(alt, az, x, y, t)$ and $C_b'^{sys}$ are wavelength-independent values that depend only on the *normalization* of the independent atmospheric and system throughputs. We can thus measure and apply corrections for the normalization of the atmospheric and hardware transmission separately, without consideration of the shape of the bandpass. We can also introduce a well-defined ‘standard’ bandpass response, $\phi_b^{std}(\lambda)$, chosen during commissioning, so that

$$\begin{aligned} C_b(alt, az, x, y, t) &= C'^{atm}(alt, az, t) C_b'^{sys}(x, y, t) \times \\ &\quad \left(\frac{\int_0^\infty f_\nu(\lambda, t) \phi_b^{obs}(\lambda, alt, az, x, y, t) d\lambda}{\int_0^\infty f_\nu(\lambda, t) \phi_b^{std}(\lambda) d\lambda} \right) \times \\ &\quad \int_0^\infty F_\nu(\lambda, t) \phi_b^{std}(\lambda) d\lambda \end{aligned} \quad (8)$$

where $F_\nu(\lambda, t) = F_o(t) f_\nu(\lambda, t)$, separating the normalization (F_o) and shape (f_ν) of the source spectral energy distribution ($m_{AB} = 2.5 \log_{10}(F_o/3631 \text{Jy})$). It’s worth noting that $\int_0^\infty F_\nu(\lambda, t) \phi_b^{std}(\lambda) d\lambda$ is a constant value for a non-variable source. For convenience, the middle term above can be written as

$$K' \left(\int f_\nu \phi_b^{obs} d\lambda \right) = \left(\frac{\int_0^\infty f_\nu(\lambda, t) \phi_b^{obs}(\lambda, alt, az, x, y, t) d\lambda}{\int_0^\infty f_\nu(\lambda, t) \phi_b^{std}(\lambda) d\lambda} \right) \quad (9)$$

where K' is a value that depends only on the *shape* of the system throughput during a particular observation and the *shape* of the SED of the astronomical object, but does not depend on the normalization of the total throughput or the total flux of the object. Note that K' simplifies to unity if the source SED, $f_\nu(\lambda)$, is constant with wavelength (i.e. a flat SED). The variation in the total counts arising from the K' term is dependent on the cumulative effect of both the atmosphere and the hardware transmission curves on the source SED, thus while the underlying wavelength-dependent (shape) variations in S_b^{sys} and S^{atm} are independent and can be measured separately, the resulting effect can only be applied as a combined correction.

Examples of the effects of variations in the $\phi_b^{sys}(\lambda)$ (hardware response) and $\phi^{atm}(\lambda)$ (atmospheric response) curves on the final observed counts are shown in Figure 2 and Table 1. Two main sequence stellar models (Kurucz 1993) – one with temperature 35000K (blue) and one 6000K (red) – were combined with three different atmospheric response curves and two different hardware response curves to illustrate the resulting changes in observed magnitudes. In Figure 3, the $X = 1.5$ atmospheric response is combined with the 1% shift

in filter bandpass (altering the hardware response) for many main sequence kurucz models, spanning a range of $g - i$ colors, and the resulting changes in observed magnitudes are plotted. These examples demonstrate that the scatter in observed magnitudes induced by expected atmospheric and hardware transmission curve shape changes alone (without any gray-scale changes) can be larger than the SRD repeatability requirements would permit. Adding variations in the gray-scale normalization due to the hardware response (typically on the order of 0.01 magnitudes) and cloud extinction (could be up to a few magnitudes) will increase the scatter in observed magnitudes.

Table 1:: Changes in observed magnitudes due to variations in system and atmospheric bandpass shape (see also Fig 2). The first two rows show the baseline ('true') magnitude of the star. All other rows show the *change* in magnitude (in mmag) due to the changes listed at left.

Bandpass	star	u (mag)	g	r	i	z	y
Standard atm, std sys	red	21.472	20.378	20.000	19.911	19.913	19.913
Standard atm, std sys	blue	19.102	19.503	20.000	20.378	20.672	20.886
		Δu (mmag)	Δg	Δr	Δi	Δz	Δy
Standard atm, +1% sys shift	red	-31	-22	-8	-2	1	1
Standard atm, +1% sys shift	blue	9	17	20	20	16	16
X=1.0, std sys	red	7	2	0	0	-0	-1
X=1.0, std sys	blue	-3	-1	-1	-0	1	-4
X=1.0, +1% sys shift	red	-24	-20	-8	-1	1	0
X=1.0, +1% sys shift	blue	7	16	19	20	18	12
X=1.8, std sys	red	-21	-10	-2	-0	0	1
X=1.8, std sys	blue	8	8	4	2	-1	6
X=1.8, +1% sys shift	red	-50	-30	-10	-2	1	2
X=1.8, +1% sys shift	blue	16	24	24	22	15	22

3.2. Model: Calibrating counts

The previous section laid out the origins of ADU count variability from one observation to another. Now we will consider how we can, in practice, acquire the information necessary to convert a particular observed ADU count to a measurement of $F_\nu(\lambda, t)$ above the

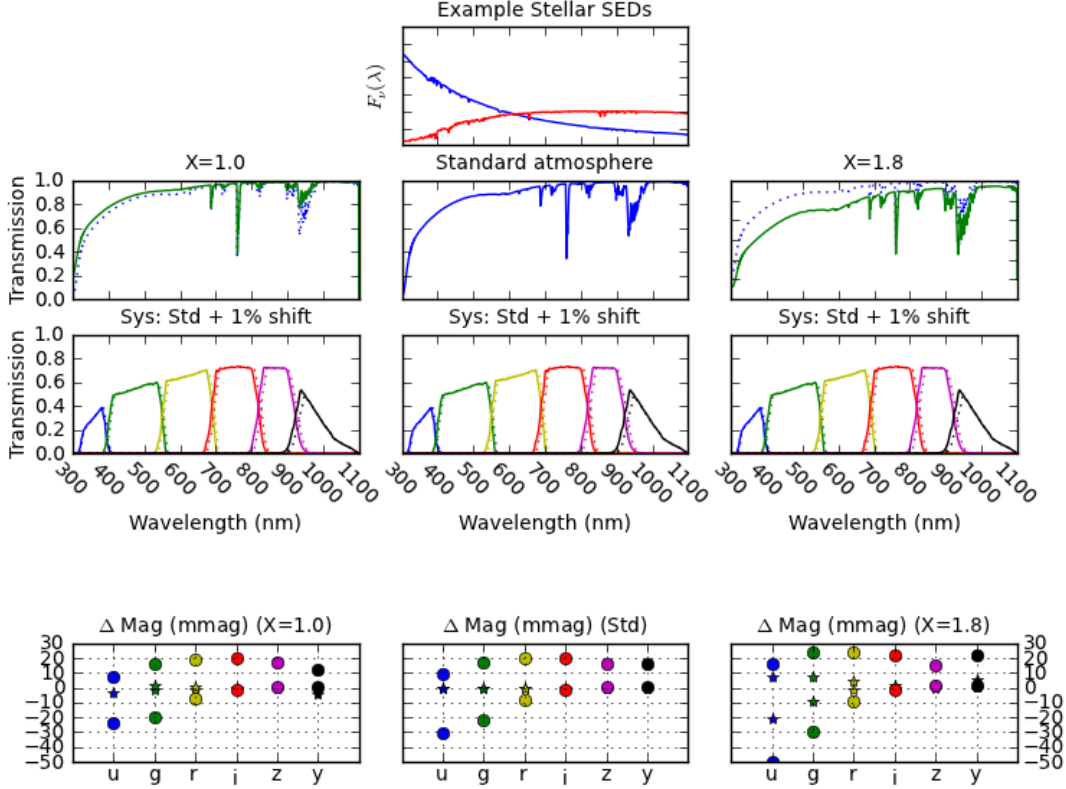


Fig. 2.—: **Changes in observed magnitudes (counts) due to variations in hardware and atmospheric bandpass shape.** Two main sequence kurucz model stars, one blue (35000 K) and one red (6000 K), were used to generate observed magnitudes (equivalent to $-2.5 \log(C_b)$ - the counts in Eqn 8) using three different atmospheric transmission profiles and two different hardware transmission profiles. The stellar flux profiles are shown in the top center panel, while the atmospheric transmission functions ($S^{atm}(\lambda)$) are shown across the second row and the two hardware transmission profiles ($S_b^{sys}(\lambda)$) are duplicated across the third row. The atmospheric transmission profiles correspond to an airmass=1.0, 1.2 and 1.8 (from left to right), with variable atmospheric absorption components. The X=1.0 atmosphere is very similar but not identical to the current LSST default X=1.2 atmosphere throughput curve, which is used as ‘standard’ here. The hardware transmission profiles consist of a ‘standard’ profile (matching the LSST current expected values) and version where the filter throughputs have been shifted by 1% of the effective wavelength of each filter (consistent with the shift expected near the edge of each filter). The final row demonstrates the changes in observed magnitudes produced by the X=1.0, ‘standard’ and X=1.8 atmospheres (left to right, respectively), combined with both the ‘standard’ hardware transmission (represented by the star points) and the +1% shifted hardware transmission (represented by the filled circles) for both the red and blue stars. The exact differences in magnitudes resulting from this calculation are listed in Table 1.

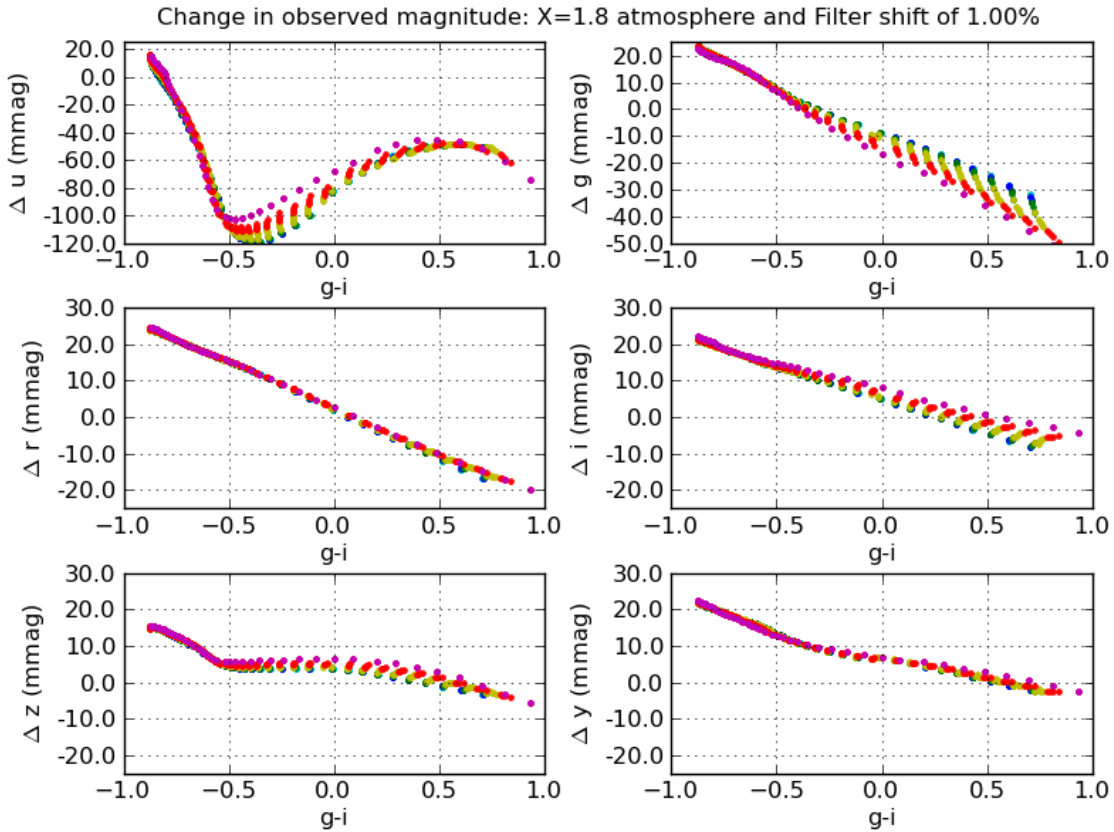


Fig. 3.—: **Changes in observed magnitudes (counts) due to a change in bandpass shape corresponding to a filter shift of 1% and an $X = 1.8$ atmosphere.** 850 Kurucz models with temperatures between 5000K and 35000K and metallicity indexes between -5.0 and 1.0 (solar) were combined with a standard system response (standard atmosphere and standard hardware bandpasses), then with a total system response where the atmosphere was replaced by an $X=1.8$ atmosphere and the filter component of the hardware transmission was shifted by 1% (as in Fig 2). It can be seen that the relationship between Δm and $g - i$ can be parameterized, although generally not with a simple linear relationship. In some cases (such as seen in the Δu and Δg panels), calculating Δm to SRD levels may require more than a simple $g - i$ color, but this is then primarily a function of metallicity which is possible to determine given the $u - g$ color in addition to the $g - i$ information. The points in each plot are color-coded by metallicity, in steps of 1 dex between -5.0 (blue) to 1.0 (magenta).

atmosphere for a particular object. In other words, how we can recreate the ‘truth’ by compensating for the variations in $S^{atm}(\lambda, alt, az, t)$ and $S_b^{sys}(\lambda, x, y, t)$, using the separability of the normalization and shape of the total system response.

Let us first consider measurement of the variations in $S_b^{sys}(\lambda, x, y, t)$. By using a dome-screen system that is capable of producing light at a range of individual wavelengths, we can measure the sensitivity of the hardware (mirrors + lenses + filter + detector) transmission as a function of x, y at each wavelength, producing a data cube of ‘narrow band flat fields’. At a particular x, y location, this data cube records the shape of the transmission response in λ (measuring $\phi_b^{sys}(\lambda, t)$). By flattening the data cube through the λ axis using a chosen spectral energy distribution, the resulting 2-dimensional (x, y) ‘synthetic flat field’ records the normalization of $S_b^{sys}(x, y, t)$. Generation of the synthetic flat field in this manner is time-consuming (requiring many hours to scan through all 6 filters at the necessary wavelength intervals, $\sim 1nm$), however the wavelength-dependent effects are expected to vary only slowly over time, so the full narrow band flat field scan will only be repeated every 30 days. Since gray-scale normalization changes are likely to occur on a much more rapid timescale, standard white-light flat fields will also be acquired at the start and end of each night. These will be used to correct the normalization of the system response on a nightly basis, updating the synthetic flat field (which has the desired SED) for the current changes in normalization. This flat field correction is particularly important over small spatial scales, as no later calibration stage can contribute to normalization corrections at less than a few times the Point Spread Function (PSF).

It is worth noting that these flat fields (both narrow band and white-light) must themselves be corrected for the effects of pixel scale variations across the field of view, for ghosting caused by internal reflections in the camera and for the presence of stray or scattered light captured in the flat. This correction is called the ‘illumination correction’. The illumination correction will be generated by combining the measurements of the system throughput from the dome screen narrow band flats, measurements of bright, dense star fields rastered across the field of view during specialized observing sequences, and measurements of the ghost patterns at various wavelengths and incident angles obtained with the ‘camera calibration optical bench’ (CCOB). It is likely (as the ghosting pattern is wavelength-dependent) that this illumination correction will have some wavelength dependence. See Figures 5 and 6 for a visual example of the illumination correction and effect on image processing. The illumination correction is expected to be stable with time and will be remeasured only when the optical path of the telescope is altered.

Next, considering $S^{atm}(\lambda, alt, az, t)$, we will again separate the measurement of the shape of the atmospheric response and the measurement of normalization of the transmission.

The wavelength-dependent variations in $\phi^{sys}(\lambda, t)$ change smoothly over spatial scales larger than the field of view and over several minutes. By using an auxiliary telescope equipped with a spectroscope to observe bright stars with known SEDs, we can measure atmospheric absorption at a variety of positions in the sky every 5–10 minutes throughout the night. These observations are used as constraints for MODTRAN atmospheric models, generating simpler representations of the atmospheric throughput (in the form of a set of absorption components as a function of alt, az, t). These components can be interpolated to generate a wavelength-dependent atmospheric absorption profile, $S^{atm}(\lambda, alt, az, t)$, for each observation. In order to correct for the higher frequency gray-scale variations in the normalization of $S^{atm}(alt, az, t)$ due to cloud extinction, we must use the observations of stars in the images themselves, as the cloud extinction can vary up to 0.01 magnitudes on the scale of a CCD (Ivezić et al. 2007) as fast as a few minutes. This ‘self-calibration’ procedure could be thought of as creating a massive calibration ‘standard’ star catalog, where the calibration stars are all of the non-variable, main-sequence stars in the science images; the main difference is that the true magnitudes of the calibration stars have to be bootstrapped from the many different observations of the survey. The calculation of the calibration star magnitudes and the determination of the normalization for $S^{atm}(alt, az, t)$ are achieved simultaneously. First the previously described corrections for $\phi^{atm}(\lambda, t)$, $\phi_b^{sys}(\lambda, t)$ and the flat field normalization must be added to each observation, producing a ‘standardized’ magnitude for each star, and then in ‘self-calibration’, we minimize the difference between the standardized magnitude and a model magnitude,

$$\chi^2 = \sum_{ij} \left(\frac{m_{b,ij}^{std} - m_{b,ij}^{model}}{\sigma_{b,ij}^{std}} \right)^2 \quad (10)$$

where the model magnitude is derived from the best-fit ‘true’ magnitude of the calibration star and the normalization constant (zeropoint offset) for this ‘patch’ (equivalent to the size of a CCD)

$$m_{b,ij}^{model} = m_{b,i}^{best} - \delta z_{b,j}. \quad (11)$$

This produces best-fit magnitudes for the calibration star catalog as well as zeropoint offsets (normalization constants) for each CCD in every observation. This procedure can also correct for variations in the normalization of the total system throughput beyond those contributed by cloud extinction, but will not be sensitive to changes on scales smaller than a patch. This is similar in nature to the ubercal method applied to SDSS in Padmanabhan et al. (2008).

Using Equation 8, we can define a ‘natural magnitude’

$$\begin{aligned} m_{nat} &= -2.5 \log_{10} \left(\int_0^\infty F_\nu(\lambda, t) \phi_b^{std}(\lambda) d\lambda \right) \\ &= -2.5 \log_{10} \left(\frac{C_b(alt, az, x, y, t)}{C'^{atm}(alt, az, t) C'^{sys}_b(x, y, t) K' \left(\int f_\nu \phi_b^{obs} d\lambda \right)} \right) \end{aligned} \quad (12)$$

(13)

describing the quantity we wish to derive from the measured ADU counts. The natural magnitudes can be related to the corrections just described above by

$$\begin{aligned} m_b^{nat} = & -2.5 \log_{10}(C_{b,raw}(alt, az, x, y, t)) \\ & + \delta z_b^{ff}(x, y, t) + \delta z_b^{selfcalib}(alt, az, t) \\ & + \delta k_b^{atm+sys}(alt, az, x, y, SED, t), \end{aligned} \quad (14)$$

where δz_b^{ff} comes from the normalization constant derived from the illumination-corrected synthetic flat field, updated for variations in normalization on a night-to-night basis by the white-light flat (and applied directly to the science images at the pixel level in the traditional manner), $\delta z_b^{selfcalib}$ comes from the normalization constant derived from the self-calibration method, and $\delta k_b^{atm+sys}$ depends on the shape of the total system response (atmosphere + hardware measured from the auxiliary telescope and the narrow band flat fields) as well as the shape of the source SED. The color-term correction $\delta k_b^{atm+sys}$ is effectively a lookup table for each observation, where $\phi_b^{sys}(\lambda, x, y, t)$ and $\phi^{atm}(\lambda, alt, az, t)$ are combined with a series of model SEDs and the resulting magnitude variation is recorded as a function of source SED and x, y in the focal plane (as the atmospheric variation is roughly constant across the field of view). For many sources (but not calibration stars) LSST will simply assume a flat SED, at which point the $\delta k_b^{atm+sys}$ correction becomes zero, and users may create their own SED and correction tables based on their knowledge of the true SED (see Appendix B).

These natural magnitudes are calibrated for variations in the observed bandpass shape (where applicable) and normalization, thus are directly comparable from one observation to another. However, they are not tied to an external physical scale (or from one filter to another), and thus only define an internally calibrated LSST magnitude in a particular filter.

To fulfill SRD requirements 3 and 4, these internally calibrated natural magnitudes must be tied from one filter band to another, and then tied to an absolute external physical scale. For this, a further set of measurements is needed. In all filters, a set of objects with a well-known spectral type (such as main sequence stars or white dwarfs, preferably with direct observations of the SED of the specific object) must be observed and calibrated, in individual filters, as above. The prior knowledge of each SED is combined with the standard bandpass shape to generate synthetic color photometry. These synthetic colors are then compared with the calibrated measured natural magnitudes to calculate Δ_{b-r} , the corrections needed to tie measurements in each filter together (referenced to r band). At this point, only one final measurement is necessary to tie the entire system to an external physical scale: an r band LSST natural magnitude measurement of an absolutely calibrated source on a photometric night. Although in theory these last two steps could be done with

a single externally calibrated object, on a single photometric night, a larger set of external reference objects with well known AB magnitudes will be used to reduce systematic errors. This defines an AB magnitude,

$$m_b^{AB} = m_b^{nat} + \Delta_{b-r} + \Delta_r \quad (15)$$

which can be compared to absolute physical flux scales.

The sequence for photometric calibration is then:

1. Acquire narrow band flat fields on a monthly basis, acquire white-light flat fields to update the narrow band flat fields on a nightly basis, and generate an illumination correction on a many-monthly basis. Apply the illumination correction to the narrow band flat fields and combine the narrow band flat fields into a synthetic flat using a chosen SED (perhaps mimicking the night sky SED). Scale the synthetic flat for any measured changes in the white-light flat occurring since the generation of the synthetic flat. Apply final synthetic flat to images directly, dividing science images by the synthetic flat field.
2. After remaining image processing (bias correction, fringe correction, etc) extract ADU counts of sources from images.
3. Acquire spectra of known stars on a 5–10 minute timeline throughout each night, fit for atmospheric absorption coefficients and generate atmospheric response curve for each science image’s alt, az, t based on MODTRAN models, retrieve hardware response curve from narrow band flat fields at various x, y locations within the focal plane. Using a range of model SEDS, generate a table of $k_b^{atm+sys}(x, y, SED)$ corrections for each observation. Apply $k_b^{atm+sys}$ corrections to stars chosen for self-calibration.
4. At appropriate intervals (such as at Data Release), minimize χ^2 from Equation 10 for the self-calibration stars and record $\delta z_b^{selfcalib}$ for each patch (each CCD in each observation).
5. Apply $\delta z_b^{selfcalib}$ to all stars in calibration patch. If an SED is known or has been chosen for particular science targets, apply appropriate $k_b^{atm+sys}$ correction.
6. Apply measured corrections Δ_{b-r} and Δ_r .

resulting in calibrated m_b^{AB} values in a standardized bandpass shape, with above-the-atmosphere fluxes.

4. The internal calibration process

The next subsections expand on each of the photometric calibration steps leading to natural magnitude and standard magnitude measurements described above, including how each correction is measured, calculated and applied. The steps described in this section are applied to each filter independently. The end result of the internal calibration process is a record of m_b^{nat} and $\phi_b^{sys+atm}(\lambda)$ measured for each object in each observation. In addition, there will be a reported spectral energy distribution (SED) assumed for each object ($f_\nu(\lambda)$) and an associated m_b^{std} that is the natural magnitude corrected for variations in the bandpass shape. In cases where the assumed SED is flat, m_b^{std} will be equal to m_b^{nat} .

4.1. Normalization of the hardware transmission

Compensation for variations (in x, y, t) in the normalization of the hardware transmission (S_b^{sys}) will be done using a flat field measured using narrow band and white light flat fields, after these are corrected for differences in illumination patterns between the dome screen and the night sky (the ‘illumination correction’). This is the first step in photometric calibration and is necessary to correct for variations in the normalization of S_b^{sys} that are smaller than a few times the PSF (and in the current calibration implementation, smaller than the scale of a CCD).

The specialized hardware for this flat field measurement is an array of projectors mounted in the dome of the LSST enclosure instead of the traditional ‘dome screen’. These projectors will be illuminated with both broadband (e.g. quartz lamp) and tunable narrow band (essentially monochromatic) light sources. Adjustment of the wavelength of the tuneable narrow band light source can be as fine as 1 nm. The projectors are designed to fill the LSST etendue with a uniform illumination, smoothly varying by less than 1% across the camera field of view (corresponding to less than 10% variability across the projector surface) and less than 0.25% on scales smaller than 0.5° (a little larger than the size of a CCD). The projectors will also be designed to limit the extent of light emitted outside the range of angles seen by the camera to reduce stray light in the flat fields (Gressler et al. 2010). A set of precision diodes will be used to normalize the photon flux integrated during flat field exposures, thus allowing a precise comparison of the system response at different wavelengths when using the narrow band light sources. These photodiodes, together with their read-out electronics, will be calibrated at the U.S. National Institute of Standards (NIST) to $\approx 0.1\%$ relative accuracy across wavelengths from 450 nm to 950 nm. The response of these diodes varies smoothly across this range of wavelength and provides a well-behaved reference for determination of $S_b^{sys}(\lambda)$. Further details of the LSST narrow band flat field apparatus can

be found in Gressler et al. (2010). Preliminary results from a similar apparatus tested at PanSTARRS can be found in Stubbs et al. (2010), as well as earlier experiments from CTIO described in Stubbs et al. (2007a).

In each filter, a set of narrow band flats will be taken at a series of wavelengths to form a data cube of flat fields in (x, y, λ) . Using the photodiode measurements of the light emitted at each wavelength, the data cube can be collapsed to a single ‘synthetic flat field’ image (x, y) by choosing a desired spectral energy distribution, then combining the individual narrow band images after applying an appropriate illumination correction (see subsection 4.1.1 for details on the illumination correction) for each wavelength and weighting by the goal SED and the photodiode measurements. The desired SED could be a single, constant SED or could be a set of SEDS, but will be clearly defined during the commissioning period. One choice might be a night sky SED to match the majority of pixels in each image; the goal SED would then vary throughout the lunar cycle.

The narrow band flats are time-consuming to acquire. Scanning through all 6 filters at 1 nm intervals requires many hours worth of exposures, but must also be done in minimal levels of ambient light. Luckily, any wavelength dependent variations in the synthetic flat are expected to change relatively slowly so the full set of narrow band flats only need to be acquired approximately once a month, which could be done during cloudy nights. However, gray-scale variations in the hardware normalization (due to dust particles on the filters, etc.) will occur on a much shorter timescale. Thus, it is necessary to use a standard white-light flat to correct for these short timescale gray-scale variations in the system throughput. The white-light flat fields will be obtained with the same apparatus as the narrow band dome flats, but as the number of exposures required to characterize a filter is dramatically reduced, these white-light flats can be obtained at the start and end of every night of observing.

The white-light flat is not applied directly to images, as it does not have the desired spectral energy distribution. Instead, changes in the white-light flat from night to night will be transferred to the data cube of narrow band flat fields, adjusting the narrow band flats for small-scale changes in gray-scale throughput. This can be done by taking a white-light flat simultaneously with the acquisition of the narrow band flat data cube. White-light flats obtained over the next month are compared to the ‘simultaneous’ white-light flat, and then the narrow band flat data cube can be multiplied by any observed differences.

The illumination pattern and color of the quartz lamp must be stable over the time interval between monthly narrow band flat measurements, to reduce changes in ghosting or color-dependent sensitivity variations in the white light flats.

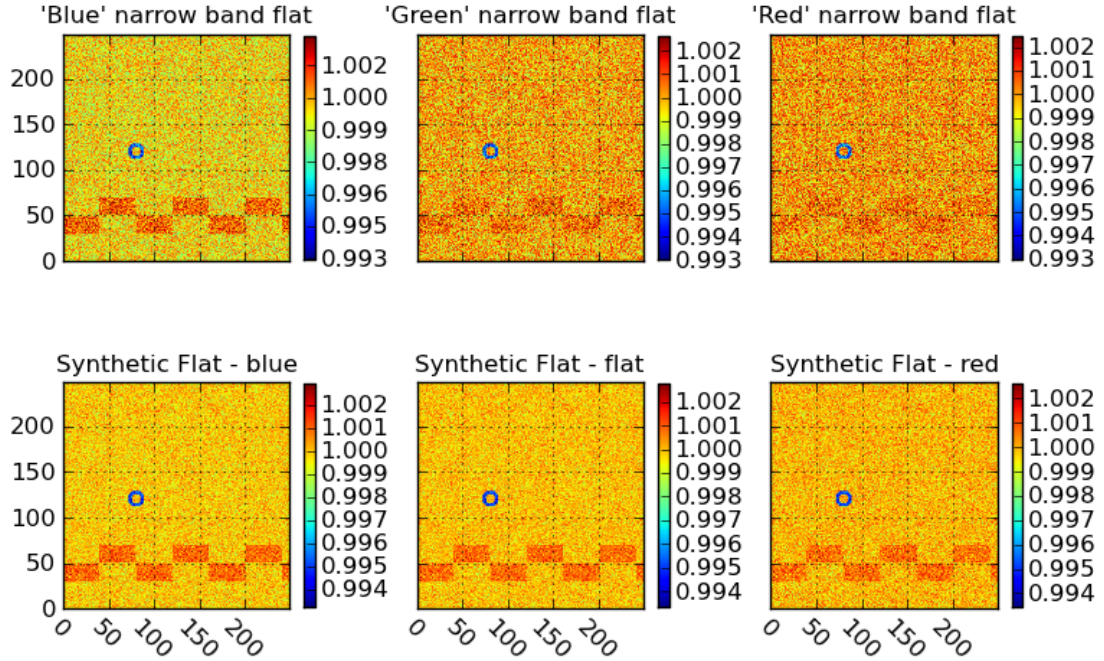


Fig. 4.—: **Simplified examples of synthetic flat generation.** The top panel illustrates simplified narrow band flats, at 'blue', 'green' and 'red' wavelengths. These represent illumination corrected (thus the relatively flat illumination pattern!) narrow band flat fields, where the detector shows a sensitivity pattern that is more pronounced in the blue wavelength flat field. The bottom panel shows the result of combining these flats to create a synthetic flat with a desired SED that is either weighted toward blue wavelengths ($1.5 \times \text{blue} + 1.0 \times \text{green} + 0.5 \times \text{red}$), a completely even distribution, or a synthetic flat weighted toward red wavelengths ($0.5 \times \text{blue} + 1.0 \times \text{green} + 1.5 \times \text{red}$). In operations, the synthetic flat will be created using a well-defined SED that will best correct the system normalization for science targets in the field.

4.1.1. Generating the illumination correction

The ideal flat field would demonstrate the hardware response to a focal plane illuminated exactly as it would be with a dark night sky, empty of ghosts, glints, stray or scattered light - recreating the hardware sensitivity variations across the focal plane as well as the effects of vignetting, both of which must be accounted for in the science images. The measured flat field, however, not only contains the actual vignetting and hardware sensitivity variations but also variations in the actual illumination pattern of the dome screen projectors, stray light, ghost images of the dome screen, and the effect of pixel scale variations across the field of view, which must be removed using the illumination correction.

The dome screen projectors will be designed to be uniformly illuminated to 1% over the focal plane, but this is already beyond the SRD specifications for photometric uniformity. There will be also light scattered within the camera dewar and some fraction of the light within the etendue will have undergone multiple reflections within the camera refractive optics (creating ‘ghost’ images of the light from the dome screen). Estimates by Photon Engineering, Inc. (Tucson, AZ) indicate that $\approx 1 - 2\%$ of the light that reaches the camera focal plane may be stray light that did not originate within the LSST etendue. In addition, projection effects cause a variation in the pixel scale from the center to the outer edges of the field of view, so that the pixels subtending a larger area (the center of the field) gather more light from the dome screen. This effect *is* present in the night sky science images as well, but does not affect the total flux measured from astronomical objects, so this gradient must be preserved in the science images (and thus removed from the flat field through the illumination correction).

Illustrative examples of these effects in a theoretical dome flat and the corresponding illumination correction are shown in Figure 5, and the effect of this illumination correct on final measured counts are shown in Figure 6.

Illumination corrections (one per filter) will be generated whenever the camera is removed from the telescope or the focal path undergoes significant changes (such as a filter being replaced or the mirrors being realuminized), but should be stable otherwise. The corrections will be created by combining information from a ZEMAX model of ghosting in the camera constrained by measurements from the Camera Calibration Optical Bench (CCOB), measurements of the observed individual narrow band dome screen (DS) flats, and dense star fields restored across the focal plane on a photometric night.

The first of these components, **Camera Calibration Optical Bench (CCOB)**, provides a method to calibrate the spatial and wavelength-dependent response of the focal plane, unmounted from the telescope, using a well controlled, wavelength-variable, light source cal-

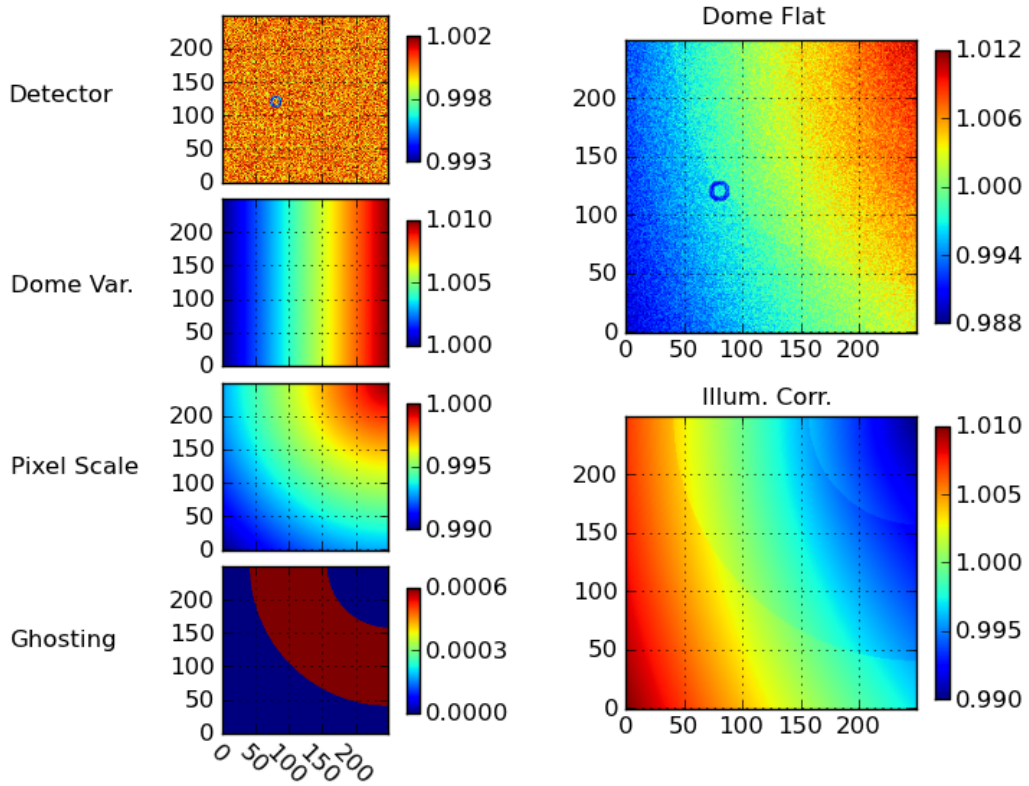


Fig. 5.—: **Components of the illumination correction.** Any flat field obtained from the dome screen includes not only a measurement of small-scale variations in detector sensitivity (Detector panel, top left), but also records unwanted effects such as variations in the dome screen illumination as a function of position (Dome Var. panel), variations in brightness that result from variations in the amount of sky observed by each pixel (arising from variations in the pixel scale over the focal plane) (Pixel Scale panel), and ghosting caused by internal reflections in the camera (Ghosting panel). Each panel on the left demonstrates the effect on the total flat field attributable to each of these variations, in a simplified manner. Variations are generated as follows: pixel-to-pixel variation in detector sensitivity is 0.4% (as well as a small dust ring), the dome screen has a 1% gradient across the field of view, the pixel scale changes by 0.5% from corner to corner, and the ghosting is generated by adding 0.1% of the total light into a ring reflection. The top large panel on the right shows the dome screen flat field that would be observed after combining all of the effects on the left. The bottom large panel on the right shows the illumination correction that must be multiplied with this flat field to remove the effects of the dome screen variation, the pixel scale variation, and the ghosting. Note that no photon noise was introduced in this simulation.

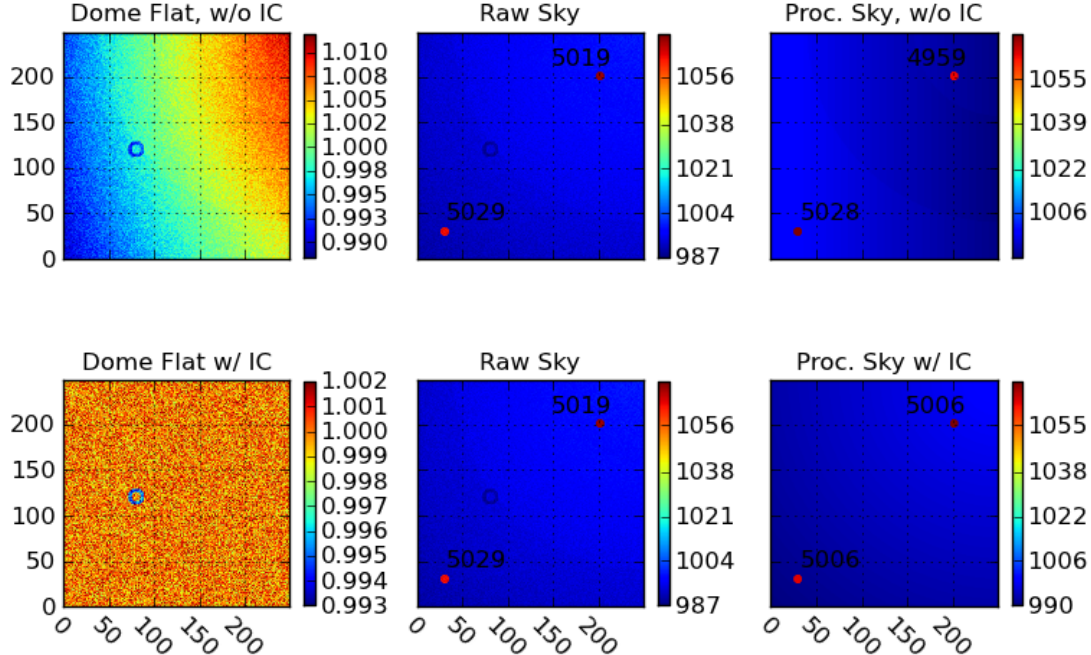


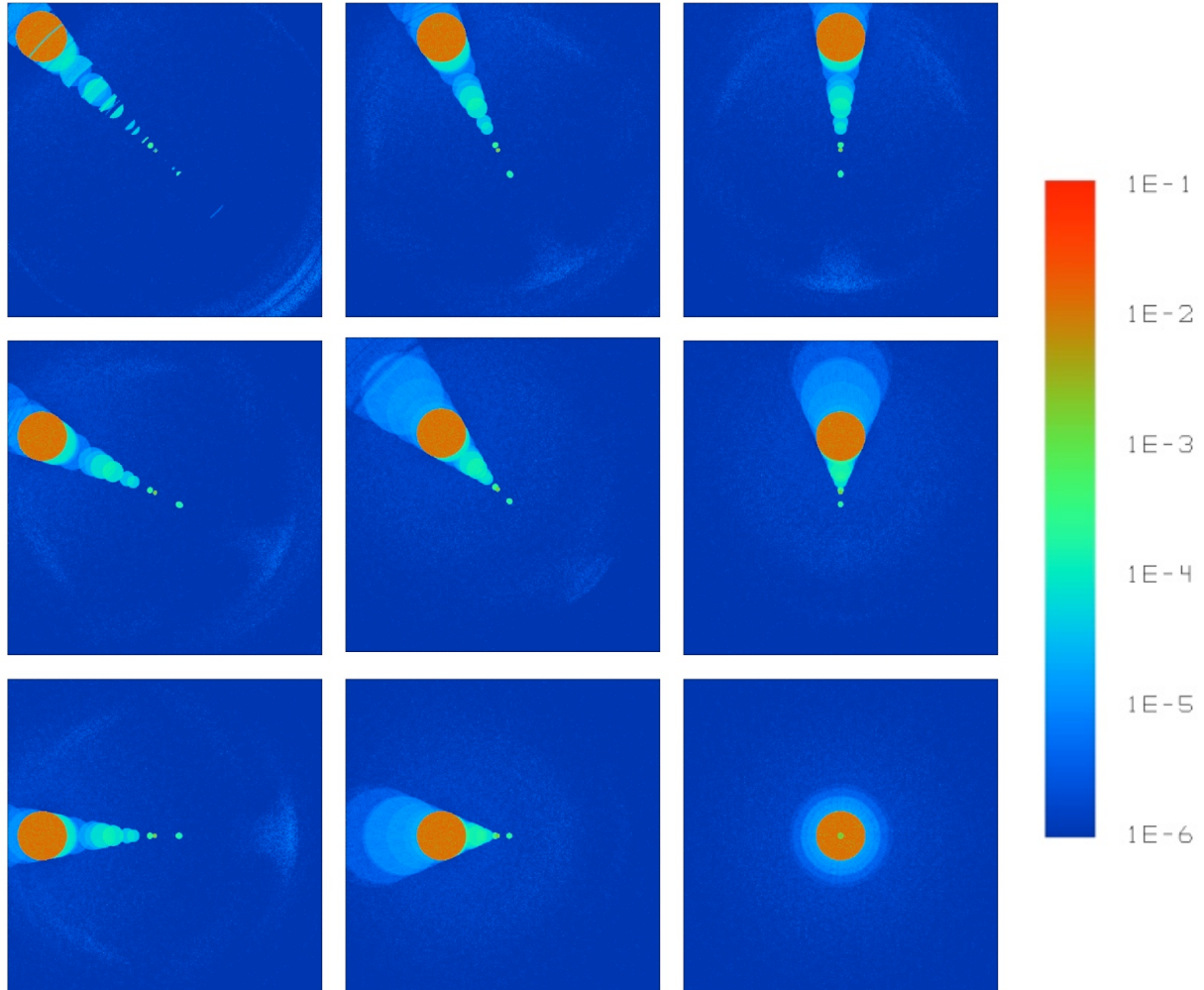
Fig. 6.—: **Effect of illumination correction on photometry.** The left top panel shows a flat field obtained from a dome screen, creating with the same conditions as in Figure 5, without multiplying by an illumination correction. The central top panel shows a raw ‘image’ of the sky, generated by adding a background sky value of 1500 counts per pixel (scaled by the pixel area, as in Fig. 5, to two stars. The stars were generated by placing 5000 counts over a circular aperture the size of the PSF at the location of the star. A ghost image was created as in Fig. 5. The right top panel demonstrates the result of processing the raw sky image by subtracting the ghost image and then dividing by the dome flat without an illumination correction. The left bottom panel shows the illumination correction applied to the same flat field. The middle bottom panel shows the same raw sky image as the top row. The bottom right panel demonstrates an improved processing of the raw sky image, by subtracting the ghost image and then dividing by the illumination corrected flat field. Note that the sky background does not appear flat but is correct for preserving stellar photometric accuracy. In every image with stars, the numbers next to each star indicate the counts measured within an appropriate circular aperture for the star. In the raw images, these counts are not equal because of the variation in pixel to pixel sensitivities.

ibrated using a NIST photodiode. This light source, which produces a spot in the focal plane approximately the size of or smaller than the PSF, will be scanned across the detector (x, y) at a variety of beam incident angles, (θ, ϕ) and at a variety of wavelengths (λ). The response of the detector will be measured in two different configurations: one with only the detector and the dewar window - which doubles as lens 3 (L3) - and one with the detector, L3, L2, L1, the filters and the camera shutter. In the L3-only configuration, the detector response should include only relative simple ghosting, primarily 3 ghost images from reflections between the CCD surface and L3. In the full refractive optics configuration (with L3, L2, L1, the filter and camera shutter), the detector response will include a more complicated ghost pattern. Current simulations indicate the strongest ghosts are expected to originate from reflections between the CCD surface and L3, where the resulting ghosts are expected to have an amplitude $5 \times \approx 10^{-4}$ relative to the flux of the source. Other ghost images, due to reflections between lens surfaces, should contain about $\approx 10^{-5}$ times the flux of the source. See Figure 7 for an example of simulated ghosting in the LSST focal plane. These measurements of the focal plane response in different optical configurations with a known incoming light source do not directly measure the illumination correction (for example, neither pixel scale variation due to projection effects nor the full stray/scattered light from the dome projectors are included), but it does provide constraints for model calculations (such as a ZEMAX model) of the illumination pattern in the camera as a function of wavelength, position in the focal plane, and beam incident angles, which are necessary for the creation of the full illumination correction, as well as constrain the focal plane response itself.

More details about the requirements and physical apparatus of the CCOB are available in LSST-10015 and LSST-8217.

The ZEMAX model describes how light scatters inside the camera creating ghosts at each wavelength. If the dome screen projectors were perfectly uniform and no stray light was scattered into the LSST etendue, the narrow band dome flats plus the predictions from the ZEMAX model would suffice to create a perfect illumination corrected synthetic flat. Stray light scattered into the LSST etendue can be modeled using work similar to that of Photon Engineering, Inc., and then the model constrained by taking measurements of the focal plane response while blacking out M2 (to image only the stray light). This creates a preliminary estimate of the illumination correction, which is particularly useful for small spatial scales (smaller than a CCD) which may not be well sampled in the next, raster-scan step.

To account for illumination variations from the dome screen projectors on large spatial scales (which could be up to 1% across the field of view), stray light scattered from other unmodeled surfaces, or systematic differences in exposure time due to the camera shutter



K. Bechtol (SLAC/KIPAC). Image from LSST Document 10008.

Fig. 7.—: **Simulations of LSST camera ghost images, as measured by CCOB.** Various beam incident angles, positions and wavelengths will be explored by the CCOB, creating focal plane measurements similar to those simulated above. These measurements will be combined to constrain a ZEMAX model describing the optical paths in the camera (including the effect of the actual coating reflectivities of the CCD and lens surfaces, etc).

movement, a dense network of stars of a variety of spectral types must be rastored across the focal plane on a photometric night. The images will be divided by the synthetic flat field corrected by the preliminary illumination correction, and then the counts for each star corrected for varying color terms in the atmosphere and hardware response, as further described in subsection 4.2. The final update to the illumination correction can then be determined by minimizing over all stars i in all observations j ,

$$\chi^2 = \sum_{i=N_{stars}, j=N_{obs}} \left(\frac{m_{ij}^{meas}(x, y) - m_{ij}^{model}(x, y)}{\sigma_b} \right)^2 \quad (16)$$

where the model magnitude of each star in each observation is given by

$$m_{ij}^{model}(x, y) = m_b, i^{best} - \delta k_{b,j}^{atm+sys}(x, y, alt, az, SED, t) - \int d\lambda dZ_{IC}(x, y, \lambda) \quad (17)$$

where $m_{b,i}^{best}$ is the best-fit, constant magnitude of the star in this filter, $k_{b,j}^{atm+sys}$ is the color-term correction (partially determined by the constant from exposure-to-exposure hardware throughput curve and partially determined by the varying with each exposure atmospheric throughput curve), and dZ_{IC} is the update to the illumination correction which is produced by this dense rastor scan. Similar applications of rastor scans have been successfully used in previous surveys, (*e.g* Regnault et al. (2009); Magnier & Cuillandre (2004); Manfroid (1996)), providing an illumination correction accurate to the sub-percent level. With the additional information from the CCOB and the better intrinsic uniformity of the dome screen illumination, we expect the illumination correction for LSST to be at least factor of 2 more accurate.

4.1.2. Error in the Normalization of the Hardware Transmission

The dome screen projectors will be designed to be uniform to be better than 0.25% (2.5 mmag) over scales less than 0.5° (slightly larger than a CCD). Translating from this engineering requirement (a strict limit) to the RMS of expected measurements implies a resulting RMS of 0.7 mmag ($=2.5 \text{ mmag}/\sqrt{12}$) in the dome illumination uniformity on scales smaller than a CCD. After using the measurements from the CCOB to model ghost reflections and scattering within the camera, the uniformity of the dome screen projectors is expected to be the limiting factor on these small scales. Applying the dense rastor scan of stars to correct for larger illumination variations from the dome screen projectors on the scale of the entire field of view, plus to correct for the effects of 1–2% stray light and systematic exposure differences due to camera shutter travel, adds an additional error of about

2.8 mmag, increasing the expected error in the illumination corrected synthetic flat field to 2.9 mmag.

The illumination corrected synthetic flats are created on a monthly basis and then must be updated for gray-scale nightly changes in the hardware transmission (due to dust,etc) using the white-light flat fields acquired using the quartz lamp in the dome screen projectors. As this update only depends on changes in the white light flats, not their absolute values, the only requirement is that the quartz lamps produce an illumination pattern in the focal plane which is stable over time at the same level as the initial illumination uniformity requirement, or stable to within 0.25% within a CCD. This means that the quartz lamps should not change their spectral profile (which may change the ghosting pattern due to wavelength dependent effects) or their illumination pattern by more than an amount which would produce changes of more than 0.25% in the focal plane, adding a further 0.7 mmag rms scatter, for a final total of 3 mmag expected error in the normalization of the hardware throughput.

4.2. Correcting for the Shape of the Hardware and Atmospheric Response Curve

Compensation for the changes in observed magnitudes caused by variations in the wavelength dependence (shape) of the hardware and atmospheric response curves, $\phi_b^{sys}(\lambda)$ and $\phi^{atm}(\lambda)$, will be done using independent measurements of the hardware response curve (generated from the narrow band flat fields) and the atmospheric response curve (generated from atmospheric extinction models generated from measurements from the auxiliary telescope). While the measurement of the shapes of the hardware and atmosphere curves are independent, the actual correction that must be applied depends on the combination of atmospheric and hardware response curves as well as the SED of the astronomical object. This correction is necessary for precision photometry, but as it requires knowledge of the object's SED, most LSST reported magnitudes will include either no correction or a (potentially rough) correction along with an indication of what SED was assumed to generate this value. However, for stars which will be used in self-calibration (see subsection 4.3) to determine photometric zeropoints in each exposure, a model SED well-matched to the object's colors will be chosen and used to generate the $\delta k_b^{atm+sys}$ corrections described in this section.

It is worth emphasizing as we start this section that $\delta k_b^{atm+sys}$ is a correction for changes in the *shape* of the bandpass only; any grayscale components to the changes in bandpass shape discussed here are not part of $\delta k_b^{atm+sys}$ and instead belong to either the hardware or atmospheric *normalization* corrections.

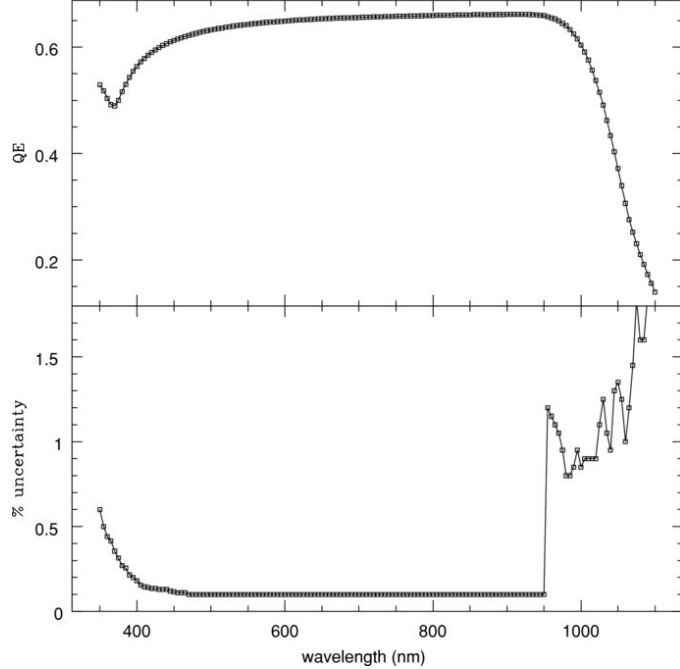
4.2.1. Measuring the shape of the hardware response curve

The hardware response curve is measured directly using the individual narrowband flat fields described in section 4.1. At each wavelength, the narrowband flat field will be illumination corrected and then used to measure the total hardware response over all x, y positions. The dome screen photodiodes will be used to track the relative intensity of the light produced by the projectors at each wavelength. These NIST-calibrated photodiodes are expected to be accurate to within 0.1% between 400-900 nm (g, r, i, z bandpasses) with current technology, which can be extended to 1600 nm (into the y band) using techniques under development (which also have the possibility of achieving 0.01% accuracy in the diode calibration at NIST) (Eppeldauer et al. 2009), as shown in Figure 8.

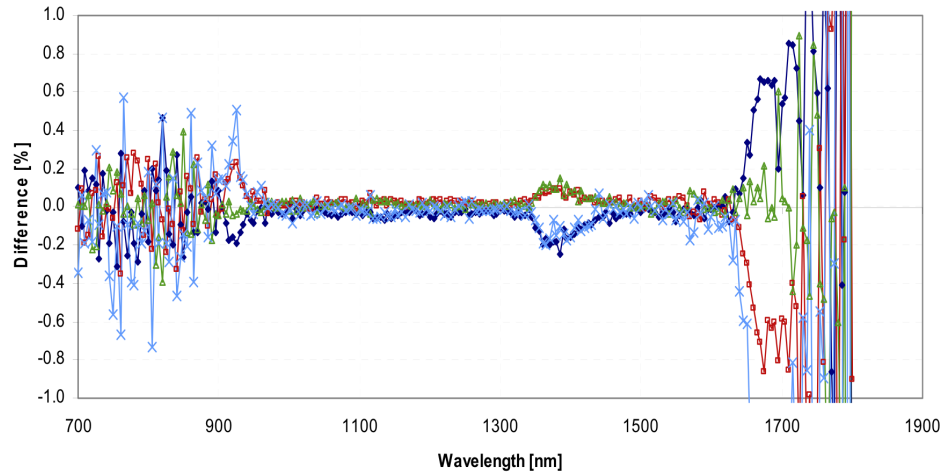
These measurements will be updated on a monthly basis, as the hardware response curve is expected to change only slowly over time due to aging in the filter and mirror coatings. It is expected that the shape of the response curve will be primarily a function of radius due to variations in the thickness of the filter coatings caused by the mechanism used to deposit those coatings. The variation due to filter nonuniformities is specified to be less than 1% across the focal plane, most likely in the form of a bandpass shift as shown in Figure 9. For main sequence stars, the resulting changes in observed magnitude as the bandpass shifts by 1% of the central wavelength can be as much or more than 0.04 magnitudes (40 mmag) – even larger in the u band (see Figure 10). However, as long as the variation in the hardware response curve is measured to better than 0.05% – equivalent to approximately a 3 Angstrom error in wavelength calibration of the monochromatic light source throughout the bandpass or a 0.5% error in photodiode calibration assuming that the shape of each bandpass is determined using at least 100 independent measurements (i.e. 1 measurement every few nanometers within the bandpass) – the maximum error contribution towards calibrating these observed magnitudes will be less than 2 mmag for all bandpasses other than u , where the error could be as much as 5 mmag for certain main sequence stars (see Figure 11).

Because the shape of the hardware response curve varies as a function of filter radius, it is also necessary to monitor any offsets of the filter position from dead center after any filter changes. Assuming the filter response curve varies linearly with radius, the filter location must be measured to better than 0.025% for the filter positioning to remain less than a 1 mmag source of error.

LJ - beamsize 100mm, plus review filter location requirement ... 0.025Plus need to include shift in bandpass due to change in incident angle ?



(a) Stubbs et al. (2010)



(b) Eppeldauer et al. (2009)

Fig. 8.—: **Quantum efficiency curve and fractional uncertainty for NIST-calibrated photodiode, from Stubbs et al. (2010) and Eppeldauer et al. (2009).** Panel (a): Between 400 and 900 nm, calibration methods already in use in test systems indicate photodiode accuracy is better than 0.1%, as in the bottom part of this panel. The sudden decrease in calibration accuracy below 900 nm is due to calibration methods used by NIST in 2005. Panel (b): More recent photodiode calibration efforts by Eppeldauer et al. (2009) show better than 0.1% accuracy can be achieved to beyond 1200 nm, the limit of detector response for LSST, as shown here in the response curves resulting from multiple scans of a single source using the same photodiode.

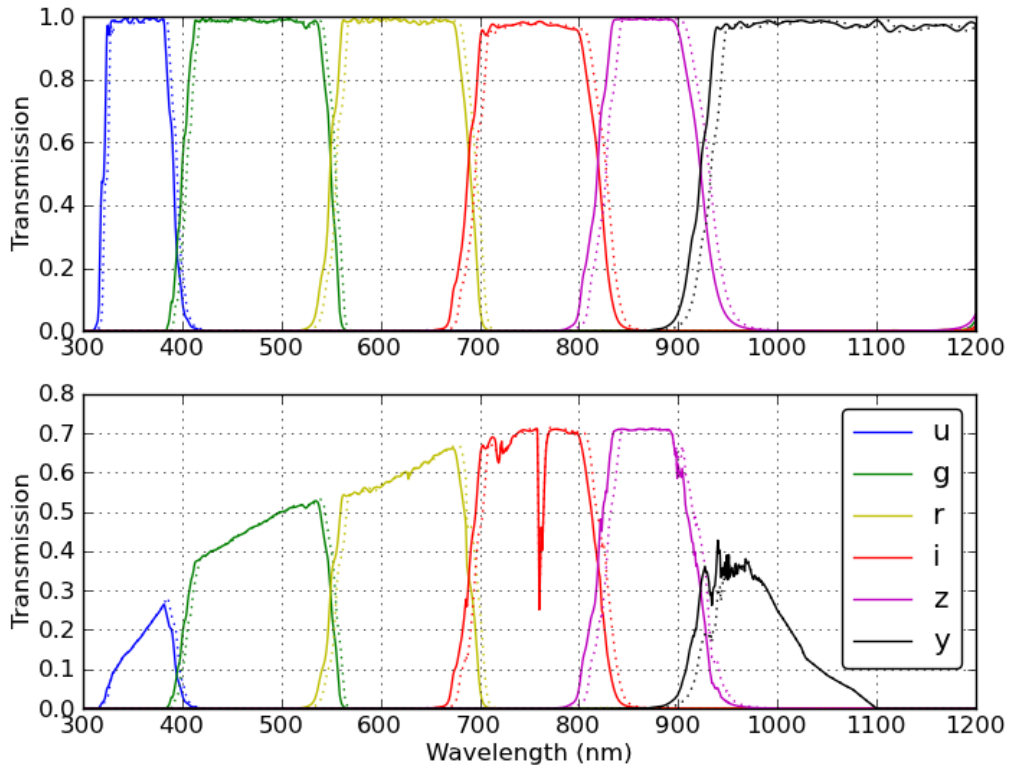


Fig. 9.—: **Baseline filter curves and a potential (1% of the central wavelength) shift due to nonuniformity.** The solid lines indicate standard filter bandpasses (top panel: filter alone, bottom panel: filter plus standard mirror, lens, detector and atmosphere response curves) while the dashed lines indicate the same bandpass shifted redward by 1% of the central wavelength.

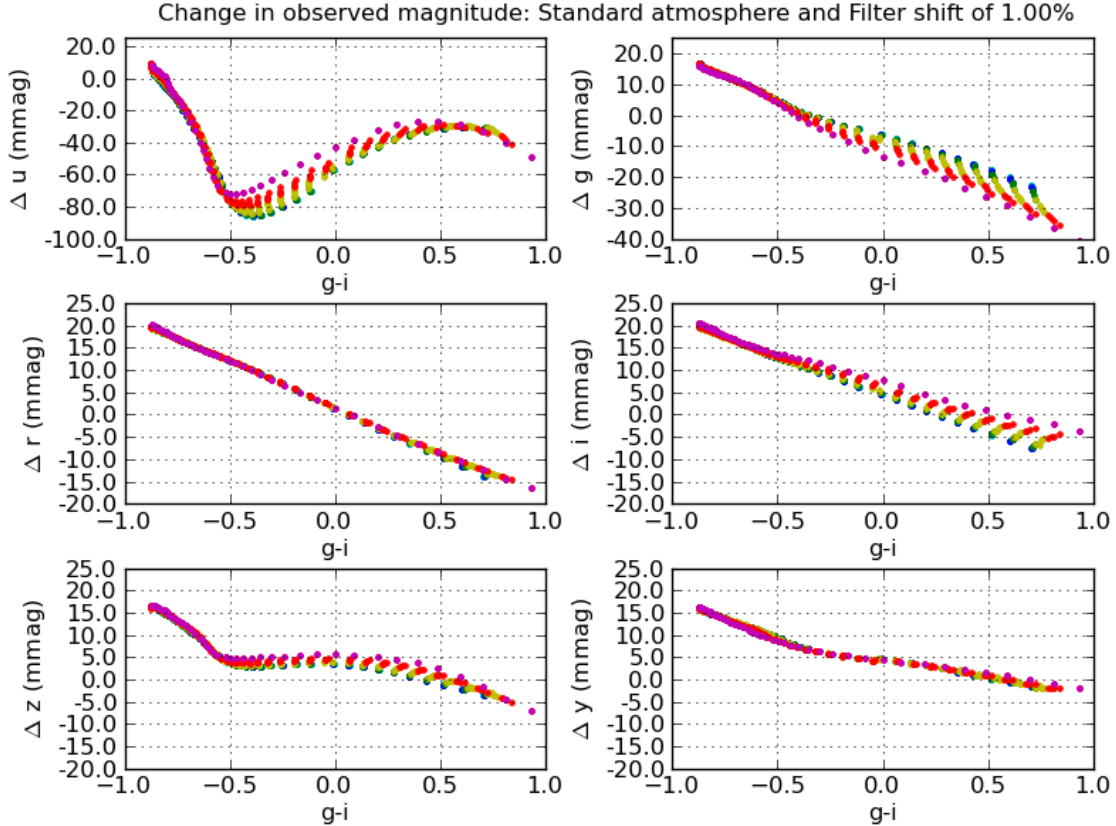


Fig. 10.—: Changes in observed magnitude (measured counts) due to a hardware response curve shift of 1% of the central wavelength of each bandpass. 850 Kurucz models with temperatures between 5000K and 35000K and metallicity indexes between -5.0 and 1.0 (solar) were combined with a standard atmosphere and standard hardware bandpass, and then with a total system response where the atmosphere remained constant but the hardware response was shifted by 1% of the central wavelength of each bandpass (as in Fig 9). Changes in magnitude on the order of 20 mmag are typical, except in u band where the shift can create a δu of closer to 80 mmag for certain kinds of main sequence stars. The points in each plot are color-coded by metallicity, in steps of 1 dex between -5.0 (blue) to 1.0 (magenta).

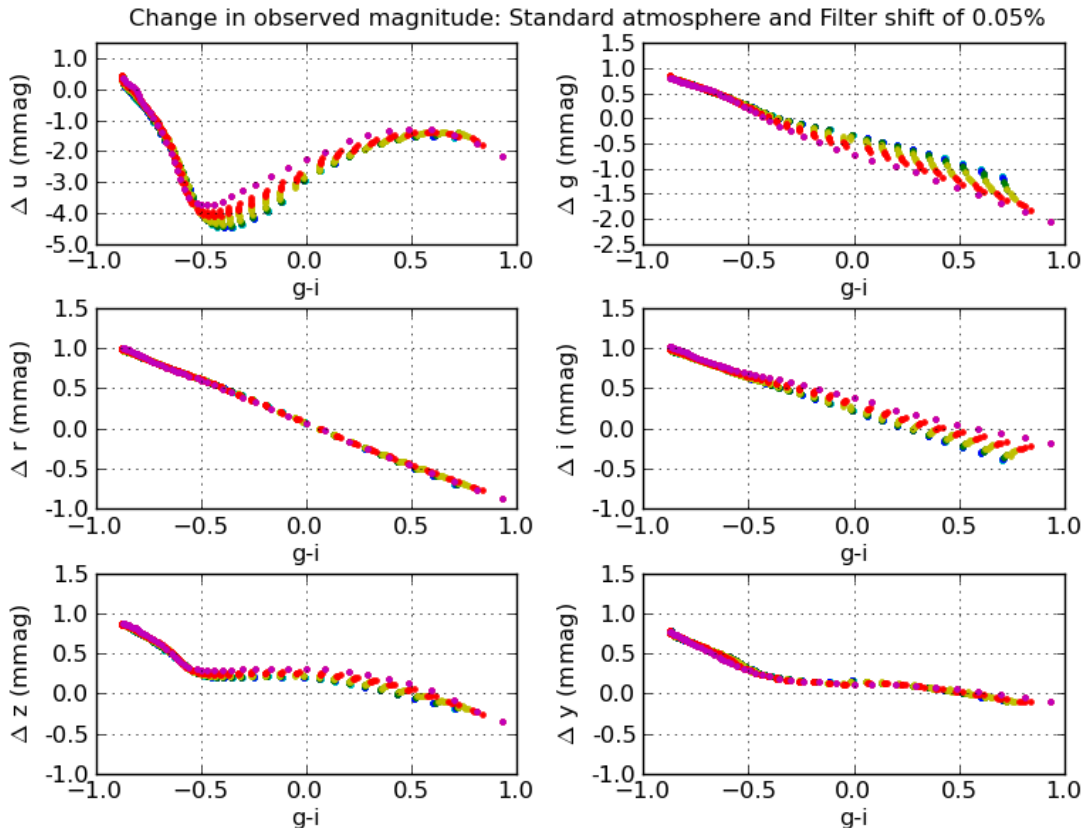


Fig. 11.—: Changes in observed magnitude (measured counts) due to a hardware response curve shift of 0.05% of the central wavelength of each bandpass. Similar to Fig 10 except that the hardware response was shifted by only 0.05% of the central wavelength, an amount representing an unmeasured shift in the hardware response and thus contributing directly to the final error in the calibration of the observed magnitudes. Note that the y scale here is 1/10th of the scale in the previous figure.

4.2.2. Measuring the shape of the atmospheric transmission curve

The shape of the atmospheric transmission curve appropriate for each observation will be generated using data from spectroscopic measurements of bright stars obtained with the LSST auxiliary telescope. These measurements will be fit to a model of atmospheric absorption extinction (which includes how this absorption varies across the sky and over time as well as atmospheric extinction profiles generated by MODTRAN (Berk et al. 1999; Anderson et al. 2001)) to determine the atmospheric transmission profile at all points on the sky at all times.

Atmospheric absorption behavior

The shape of the atmospheric transmission curve, $\phi^{atm}(\lambda, alt, az, t)$, is determined by three major sources of atmospheric extinction: molecular scattering (Rayleigh scattering), aerosol scattering (Mie scattering), and molecular absorption.

- Molecular scattering, or Rayleigh scattering, is due to elastic scattering off atoms and molecules in the air. Atmospheric absorption due to Rayleigh scattering has an optical depth

$$\tau \propto (\lambda/\lambda_o)^{-4} (BP/BP_o), \quad (18)$$

where BP is the barometric pressure (Hansen & Travis 1974), and BP_o is a reference value (typically around 782 mb for Cerro Tololo). The total atmospheric extinction due to Rayleigh scattering is thus driven only by pressure variations and is proportional to airmass,

$$S(\lambda, X) \propto e^{-\tau, X}, \quad (19)$$

and is also axisymmetric around zenith. Changes in the optical depth due to Rayleigh scattering typically will produce < 1 mmag change in the observed counts.

- Aerosol scattering, or Mie scattering, occurs when visible light is scattered by particles suspended in the atmosphere with a size similar to its wavelength. This gives rise to an absorption curve with a strongly variable total column depth as well as a variable wavelength dependence, where

$$\tau \propto (\lambda/675\text{nm})^\alpha. \quad (20)$$

The index α has been measured to range between -0.9 to -1.7 in observations from CTIO (Burke et al. 2010). From (Stubbs et al. 2007b) optical depth measurements from Mauna Loa, the total aerosol optical depth at zenith varied from 0 to 0.3 (generally ± 0.1)

at $\lambda = 440$ nm, with max rate of change $\approx 0.02/\text{hr}$. The atmospheric extinction due to aerosol scattering scales directly with airmass but is not necessarily axisymmetric around zenith and often has an East-West trend.

- Molecular absorption produces a more complex set of absorption bands and features, originating from line absorption due to ozone (O_3), water (H_2O), oxygen (O_2) and other trace species (OH , N^2O , etc.). The resulting atmospheric absorption features are largely due to narrow saturated Lorentzian-shaped lines spaced closely in wavelength and, due to this saturation, scale non-linearly with airmass,

$$S(\lambda, X) \propto e^{-\tau \sqrt{X}} \quad (21)$$

as in (Stubbs et al. 2007b). The total column depth for O_2 and other trace species is related directly to the square root of the column depth for molecular scattering, and is thus proportional only to the square root of the barometric pressure and airmass. However, O_3 and H_2O absorption is more variable. O_3 absorption can vary by 5–10% day to day, with seasonal variations of 25% or so, but is expected to be non-variable across the sky and closely correlated with satellite data on total ozone content. H_2O absorption can vary on timescales as short as 10–20 minutes, and is expected to show linear trends across the sky (East-West and North-South).

Figure 12 demonstrates the wavelength dependency of each of these components and how they change with airmass.

Fitting the atmospheric absorption

Using MODTRAN we can generate atmospheric transmission profiles at a variety of airmasses for each of these major sources of atmospheric extinction – molecular (Rayleigh) scattering, aerosol (Mie) scattering, and molecular absorption from each of O_3 , H_2O , and combined O_2 /trace species, as is shown in Figure 12 for a standard atmospheric composition (the 1976 US Standard). These profiles capture the wavelength dependence of each component individually, over a grid of airmasses, and can be used as templates to generate new atmospheric transmission curves for any desired atmospheric composition as follows:

$$\begin{aligned} S^{fit}(alt, az, t, \lambda) &= e^{-\tau_{aerosol}(alt, az, t, \lambda) X} \\ &\times (1 - C_{mol}(BP(t)/BP_o) A_{Rayleigh}(X, \lambda)) \\ &\times (1 - \sqrt{C_{mol}(BP(t)/BP_o)} A_{O_2}(X, \lambda)) \\ &\times (1 - C_{O_3}(t) A_{O_3}(X, \lambda)) \\ &\times (1 - C_{H_2O}(alt, az, t) A_{H_2O}(X, \lambda)). \end{aligned} \quad (22)$$

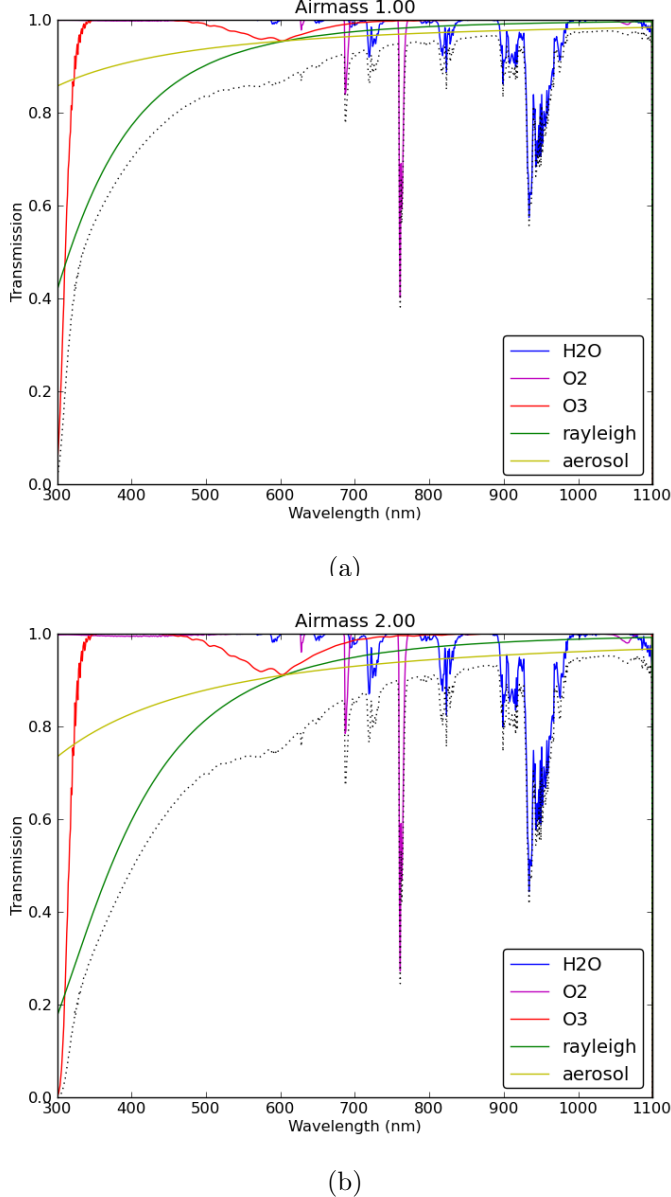


Fig. 12.—: **Components of atmospheric absorption.** The wavelength dependence of the various components of atmospheric absorption at zenith (panel a) and at airmass=2.0 (panel b) is shown here. The H₂O(blue) and O₃(red) molecular absorption contributions are shown separately, while the O₂absorption is combined with other trace elements (magenta). A typical example of aerosol scattering (Mie scattering) is included (yellow), as is molecular scattering (Rayleigh scattering) (green). All components except aerosol scattering were generated using MODTRAN4 with the US Standard option (aerosol scattering is not part of the US Standard atmosphere). The resulting total absorption curve is the product of each of these effects and is shown with the dotted black line. This is an illustrative atmosphere; under actual observing conditions the molecular absorption components will vary in strength with time and the square root of the airmass, the molecular and aerosol scattering will depend on airmass, and the aerosol scattering profile will also vary with time.

The $A_{Rayleigh/O_2/O_3/H_2O}$ functions are absorption templates (i.e. 1 minus the transmission profiles from the MODTRAN models) and the C_{mol,O_3,H_2O} are coefficients describing the composition of the atmosphere together with $\tau_{aerosol}$, and $BP(t)$ is measured. An example of an atmosphere generated in this fashion is shown in Figure 13, demonstrating that this method can be used to generate an atmosphere at any airmass for any composition desired, without needing to generate a full MODTRAN model.

With this capability, we can fit the auxiliary telescope spectroscopic data taken throughout the night for the values of C_{mol,O_3,H_2O} , increasing our SNR for these coefficients by modeling their expected behavior over time and across the sky as detailed in 4.2.2 above. The Rayleigh scattering and molecular absorption due to O₂ and other trace species are fit with a single coefficient, C_{mol} , which simply scales the MODTRAN templates to the appropriate level for Cerro Pachon, and then only change with the barometric pressure (BP). The O₃ absorption is fit with a single C_{O_3} value for each night. The aerosol absorption, as it is expected to have a small spatial variation across the sky, is modeled as

$$\tau_{aerosol}(alt, az, t, \lambda) = (\tau_0 + \tau_1 \text{EW} + \tau_2 \text{NS}) \left(\frac{\lambda}{\lambda_0} \right)^\alpha, \quad (23)$$

where EW and NS are defined as $\text{EW} = \cos(alt)\sin(az)$, $\text{NS} = \cos(alt)\cos(az)$, projections of the telescope pointing in the EW/NS directions. Single values of τ_0 , τ_1 , τ_2 and α are fit for each night of observing, with τ_1 and τ_2 likely to be very small (Burke et al. 2010). The H₂O absorption is likewise expected to show spatial variation, but also time variability, and is modeled as

$$C_{H_2O}(alt, az, t) = C_{H_2O}(t) + \frac{dC_{H_2O}}{d\text{EW}} \text{EW} + \frac{dC_{H_2O}}{d\text{NS}} \text{NS} \quad (24)$$

using a constant spatial EW and NS gradient per night and a $C_{H_2O}(t)$ that is fit to each auxiliary telescope measurement (and interpolated between these times).

The coefficients $C_{mol/O_3/H_2O}$ and $\tau^{aerosol}$ will be determined using spectra of bright stars obtained from the 1.2-m LSST auxiliary telescope. The auxiliary telescope will be equipped with a modest resolution ($R \sim 400$) spectrograph, sufficient to capture the signatures of the atmospheric extinction components, and covering the entire wavelength range of LSST ($300 < \lambda < 1100$ nm) in each exposure. The stars observed with the auxiliary telescope must be bright ($r < 12$) and ideally either white dwarfs or F stars – stars with relatively simple and well-understood SEDs to minimize confusion with the atmospheric extinction. By observing the same grid of stars on multiple nights, even if the SEDs are not well determined initially, they can be bootstrapped from the many epochs of data.

Generally, the auxiliary telescope will not observe stars along the same line of sight as LSST, as the values for $C_{mol/O_3/H_2O}$ and $\tau^{aerosol}$ are better constrained by observing a

wide variety of airmasses and locations on the sky that cover a wide range in N/S/E/W directions, as well as utilizing repeat observations of the same star throughout each night, and then fitting the spectroscopic data from the entire night.

Burke et al. (2010) describes a series of observing runs at CTIO carried out over several months, where spectroscopic observations of stars were fit using this method. Using the extremes of the range of C_{mol} , C_{O_3} , C_{H_2O} , τ_i and α parameters from these runs, Figure 14 shows the resulting changes in observed magnitudes due to the changes in bandpass shape when applied to our set of main sequence star Kurucz models. Varying C_{H_2O} only affects the z and y bands, while changing C_{O_3} , τ_0 , and α affect the u and g and, to a lesser extent, r bands. Using these ‘worst-case’ parameters, at $X = 1.2$ we find differences of $\Delta u=14$ mmag, $\Delta g=7$ mmag, $\Delta r=4.5$ mmag, $\Delta i=1.5$ mmag, $\Delta z=2$ mmag, and $\Delta y=7$ mmag. The atmosphere transmission curves used to generate this info, and a plot of the resulting changes in magnitudes are in Figures 15 and 16. These represent the induced changes in observed counts due to changes in the bandpass shape; however, by achieving 10% accuracy on $\tau^{aerosol}$, C_{O_3} , and C_{mol} , and 30% accuracy for C_{H_2O} , we can correct for these effects to within 1 mmag in all bands except y , where it remains 2 mmag. The limits on remaining uncorrected effects are shown in Figure 17.

Changes in airmass have a larger effect on observed magnitudes (Figure 18) than the variation in atmospheric extinction coefficients. However, these are included in the atmospheric extinction templates generated by MODTRAN and can be accurately corrected. Within the LSST 3.5° diameter field of view, the difference in airmass from top to bottom of the field can be considerable, and must be included in the model.

4.2.3. Errors in the shape of the hardware and atmospheric response

Correcting observed counts for the difference between the measured shape of the hardware and atmospheric response curves and the standard normalized bandpass, $\phi_b^{std}(\lambda)$, requires knowledge of the SED of each star. However, with this knowledge, it is possible to create lookup tables of $\delta k_b^{atm+sys}(x, y, alt, az, SED, t)$ (as in Equation 14) for various locations in the focal plane in each exposure. A rough example is given in Table 1.

Assuming that the errors in the combined shape of the hardware and atmospheric response curves add in quadrature, with the limits described above (2 mmag error in *grizy*, 5 mmag error in *u* due to the hardware response curve; 1 mmag in *ugriz*, 2 mmag error in *y* due to the atmospheric response curve), the final error in observed magnitude due to both of these effects would be < 3 mmag in *grizy* and 5 mmag in *u*. There is an additional

potential source of error in these $\delta k_b^{atm+sys}$ corrections – the understanding of the true SED of the source.

LJ - Generate: errors due to bad knowledge of SED

4.3. Normalization of the Atmospheric Transmission

After applying each of the previous corrections, the raw counts have been corrected to a ‘standard’ bandpass for each filter, $\phi_b^{std}(\lambda)$, using both the narrow band flats and the atmospheric model derived from the auxiliary telescope observations. Small scale (< several times the PSF) gray-scale zeropoint variations have also been removed by the synthetic flat. However, there still remain variations in the normalization of the system response that result from gray-scale extinction due to clouds. The self-calibration procedure is necessary to correct for these zeropoint offsets.

The self-calibration procedure selects bright, isolated main sequence and white dwarf stars (or any star with well-known colors and a well-known SED, to reduce errors in the applied δk values) from the sample of all observed stars after they are corrected to the standard bandpass (‘standardized’). Only non-variable stars will be selected for self-calibration, based on approximately calibrated data (say, a few percent) which will suffice in this context. It then uses the many repeat observations j of each star i in a particular filter to minimize

$$\chi^2 = \sum_{ij} \left(\frac{m_{b,ij}^{std} - m_{b,ij}^{model}}{\sigma_{b,ij}^{std}} \right)^2 \quad (25)$$

where the m_{model} includes any remaining photometric corrections that must be applied. In our current calibration plan, this would be only the gray extinction from clouds, applied by requiring the photometric zeropoint offset over a small patch of sky in a given observation, δz_j , be constant:

$$m_{b,ij}^{model} = m_{b,i}^{best} - \delta z_{b,j}, \quad (26)$$

where the patch size is approximately one CCD in size. A more complicated model, *e.g.* a δz_b with structure, could be used if found desireable. Simulations of the Milky Way based on a model by Mario Juric (JuricREF) indicate that there will be approximately 50–100 suitable calibration stars per patch over the entire sky.

Minimizing Equation 25 requires solving for approximately, $10^8 m_{b,i}^{best}$ and $10^8 \delta z_j$. Of course, not all stars will be observed on all calibration patches, so there will be only about 10^{10} non-zero values of $(m_b^{std})_{ij}$ (per band). Preliminary work using a conjugate gradient

method to compute m_b^{best} and δz_j for approximately 10^6 stars and 10^6 patches was very successful; the same method could be relatively easily parallelized for the full data set.

With the known values of $(\delta z)_j$, all measurements from that patch can be re-calibrated, then analyzed for systematics in $[(m_b^{std})_{ij} - (m_b^{best})_i]$ and $[(m_b^{obs})_{ij} - (m_b^{best})_i]$ residuals (e.g., as a function of observation time, position on the focal plane, airmass, seeing, stellar color, brightness, seeing, etc.). The self-calibration step can be repeated if necessary, with corrections for systematics incorporated in the next-iteration values for $(m_b^{std})_{ij}$ or added directly into the model magnitudes used for the self-calibration solution. Thus this step provides a potential avenue for improvement in errors introduced at earlier stages (such as a mis-measurement of the atmospheric throughput or flat-field).

The self-calibration step can be successful only if patches overlap on the sky so that the same star is observed on multiple patches. It is good to note that $(m_b^{best})_i$ and $(\delta z)_j$ are constrained only up to an arbitrary additive constant. For convenience, this constant can be set so that stars have roughly correct AB magnitudes, however the goal after self-calibration is only to have a rigid, self-consistent magnitude system, equivalent to the natural magnitudes.

More details of the self-calibration procedure can be found in Docushare Document-8619 and Jones 2010 (SPIE paper).

LJ - there is more to go here. Perhaps figure with milky way density in all bandpasses. Definitely more info from more recent sims that follow error distribution up to this point. Also describe some limits to selfcal.

5. Fixing LSST to an external scale

The next two subsections describe how the internally calibrated natural magnitudes, independently calibrated in each filter bandpass, are fixed to an external scale such that the flux in a single band can be compared to the flux in another filter band (SRD requirement 3) and that the flux in a particular filter band can be compared to an absolute external system (SRD requirement 4). This is equivalent to determining Δ_{br} and Δ_r from Eqn 15.

5.1. Band to band (color)

The band to band calibration for each filter b (the Δ_{br} values) will be determined by measuring the flux from one or more celestial objects whose physics and chemistry are

believed to be well understood. In principle, a single object with known colors would be sufficient, however many objects across the LSST footprint will be used to evaluate possible systematic effects in the internal calibration process.

Hot hydrogen (DA) and helium (DB) white dwarf stars have simple atmospheres that are reasonably well understood (model colors are currently reliable to about 0.01 magnitudes). It is estimated that there will be $\approx 100/10$ DA/DB WD stars with $r < 24$ in each LSST image at the South Galactic Pole. Catalogs of WD stars visible from Cerro Pachon have been constructed (Bergeron 1992, Eisenstein 2006), and a ‘white dwarf calibration system’ has been developed (Holberg & Bergeron 2006). The locus of main sequence stars in color-color space is also reasonably well understood and has been used to calibrate photometry with success in previous surveys (MacDonald 2004, Ivezić 2007). The use of the main sequence stellar locus in addition to WD stars will provide a valuable check on systematic effects that may arise from using (primarily) white dwarfs in the determination of $\phi^{atm}(\lambda, alt, az, t)$.

The values for Δ_{br} will be determined by generating model m_b^{nat} values for each band-band calibration object, then minimizing

$$\chi^2 = \sum_i \left(\frac{(m_{b,i}^{nat} - m_{r,i}^{nat})^{meas} - (m_{b,i}^{nat} - m_{r,i}^{nat})^{model}}{\sigma_{b-r,i}} \right)^2. \quad (27)$$

This comparison can be done using subsets of objects from low galactic extinction regions, and then bootstrapping to the entire sky to check for systematic effects, perhaps by using the main sequence stellar locus as an additional method to determine the amount of galactic extinction.

LJ - there is more to come here, based on notes from Zeljko. Include stellar locus / quasar locus / white dwarf locus and how this can help constrain band-to-band color variations (particularly with different sensitivities to dust)

5.2. Single bandpass to external flux system (absolute scale)

After determining the band to band calibration, there is a single number required to calibrate the entire system to an absolute flux scale: Δ_r . This can again be determined using a single object with a well-known flux and spectral energy distribution, however multiple external calibrators provide a valuable check on systematic effects.

Several WDs in the Northern hemisphere have been very precisely calibrated with HST STIS measurements (Bohlin & Gilliland 2004) and it should be possible to obtain similar HST measurements of one or more targets for use in the Southern hemisphere. Identification

of these targets has not yet been done.

REFERENCES

- Anderson, G. P., et al. 2001, in Society of Photo-Optical Instrumentation Engineers (SPIE) Conference Series, Vol. 4381, Society of Photo-Optical Instrumentation Engineers (SPIE) Conference Series, ed. S. S. Shen & M. R. Descour, 455–459
- Berk, A., et al. 1999, in Society of Photo-Optical Instrumentation Engineers (SPIE) Conference Series, Vol. 3756, Society of Photo-Optical Instrumentation Engineers (SPIE) Conference Series, ed. A. M. Larar, 348–353
- Burke, D. L., et al. 2010, *ApJ*, 720, 811
- Eppeldauer, G. P., Yoon, H. W., Zong, Y., Larason, T. C., Smith, A., & Racz, M. 2009, *Metrologia*, 46, 139
- Gressler, W. J., Doherty, P., Krabbendam, V. L., Liang, M., Saha, A., Stubbs, C. W., & Vaz, A. 2010, in Presented at the Society of Photo-Optical Instrumentation Engineers (SPIE) Conference, Vol. 7739, Society of Photo-Optical Instrumentation Engineers (SPIE) Conference Series
- Hansen, J. E., & Travis, L. D. 1974, *Space Sci. Rev.*, 16, 527
- Ivezić, Ž., et al. 2007, *AJ*, 134, 973
- Kurucz, R. L. 1993, *VizieR Online Data Catalog*, 6039, 0
- Magnier, E. A., & Cuillandre, J. 2004, *PASP*, 116, 449
- Manfroid, J. 1996, *A&AS*, 118, 391
- Padmanabhan, N., et al. 2008, *ApJ*, 674, 1217
- Regnault, N., et al. 2009, *A&A*, 506, 999
- Stubbs, C. W., Doherty, P., Cramer, C., Narayan, G., Brown, Y. J., Lykke, K. R., Woodward, J. T., & Tonry, J. L. 2010, *ApJS*, 191, 376
- Stubbs, C. W., et al. 2007a, in Astronomical Society of the Pacific Conference Series, Vol. 364, The Future of Photometric, Spectrophotometric and Polarimetric Standardization, ed. C. Sterken, 373–+

Stubbs, C. W., et al. 2007b, PASP, 119, 1163

A. Filter Set

B. Improvements in photometric accuracy

To conduct science with the catalogs from LSST, the natural magnitudes, m_b^{nat} , for each astronomical object in each visit must obviously be recorded, resulting in approximately 2×10^{13} measurements. However, in order to permit scientists to generate higher precision photometry for objects with known SEDs (which are likely to be different than the SEDs LSST used to create those m_b^{nat} measurements), $\phi_b^{meas}(\lambda, alt, az, x, y, t)$ and the zeropoint offset from the self-calibration procedure must also be available. With these additional pieces of information, scientists can generate more precise $\delta k(alt, az, x, y, SED, t)$ corrections to m_b^{nat} .

For many objects, LSST will assume a flat SED when generating m_b^{nat} values, implying that no $\delta k(alt, az, x, y, SED, t)$ correction was applied. Sections 4.2.1 and 4.2.2 outline the typical magnitudes of these corrections; for some main sequence stars these corrections can easily be on the order of 20 mmag for *gri*, or even 100 mmag in *u* band. For more extreme SEDs, these corrections may be even larger.

CREATE FIGURE: the likely magnitude of these corrections

Data management could record a full $\phi_b^{meas}(\lambda, alt, az, x, y, t)$ value for every object in every visit, where the resolution on $\phi(\lambda)$ will need to be at least 0.5 nm. It should also be possible for data management to simply record the full narrow band flat field data cube, the SED used to create the synthetic flat field, the interpolated components for the atmosphere (approximately 6 parameters per visit), and the zeropoint applied to each patch (approximately 369 per visit). Together with provenance information on how each of these was used to generate the observational corrections, it would then be possible to regenerate a higher precision m_b^{nat} .

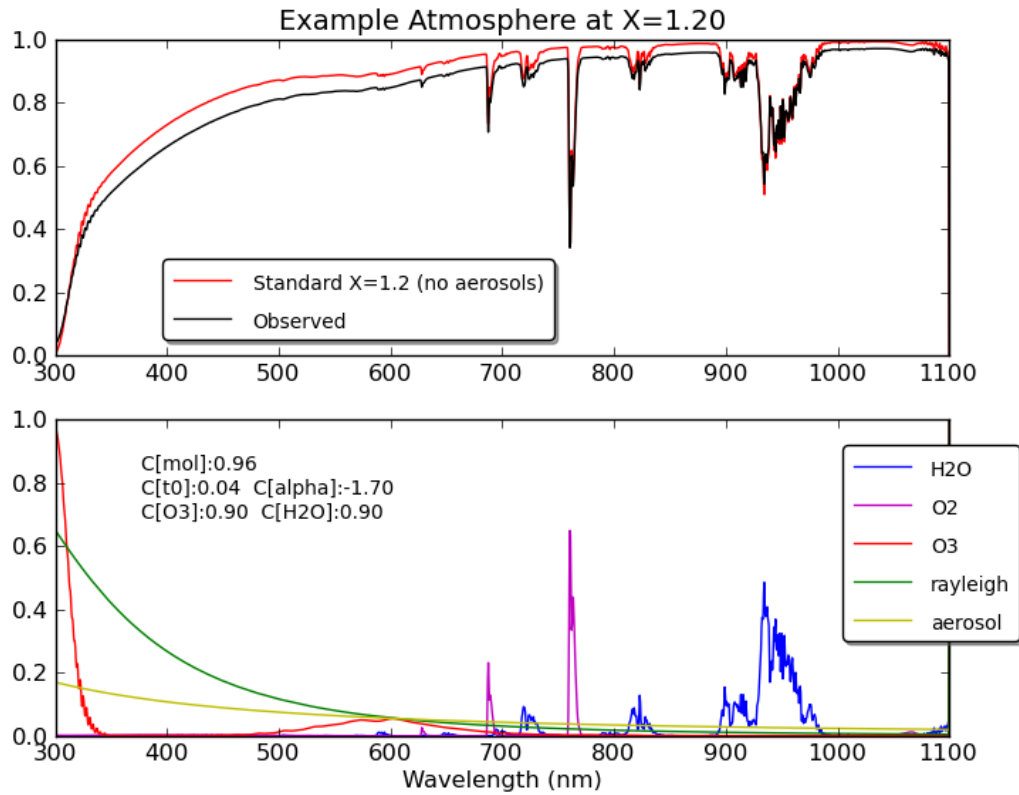


Fig. 13.—: **Example of an atmosphere generated from a typical mix of atmospheric components.** The bottom panel shows the MODTRAN absorption templates at this airmass used in generating the final atmosphere (the $A_{\text{rayleigh}/\text{O}_2/\text{O}_3/\text{H}_2\text{O}}$ and $A_{\text{aerosol}} = 1 - e^{\tau_{\text{aerosol}}}$ from Equation 22). The top panel shows the final combined atmospheric transmission curve in black, as well as a ‘standardized’ atmospheric transmission curve in red. This demonstrates that (even without using the full MODTRAN software, just the transmission templates) that we can closely recreate any atmosphere desired with any composition.

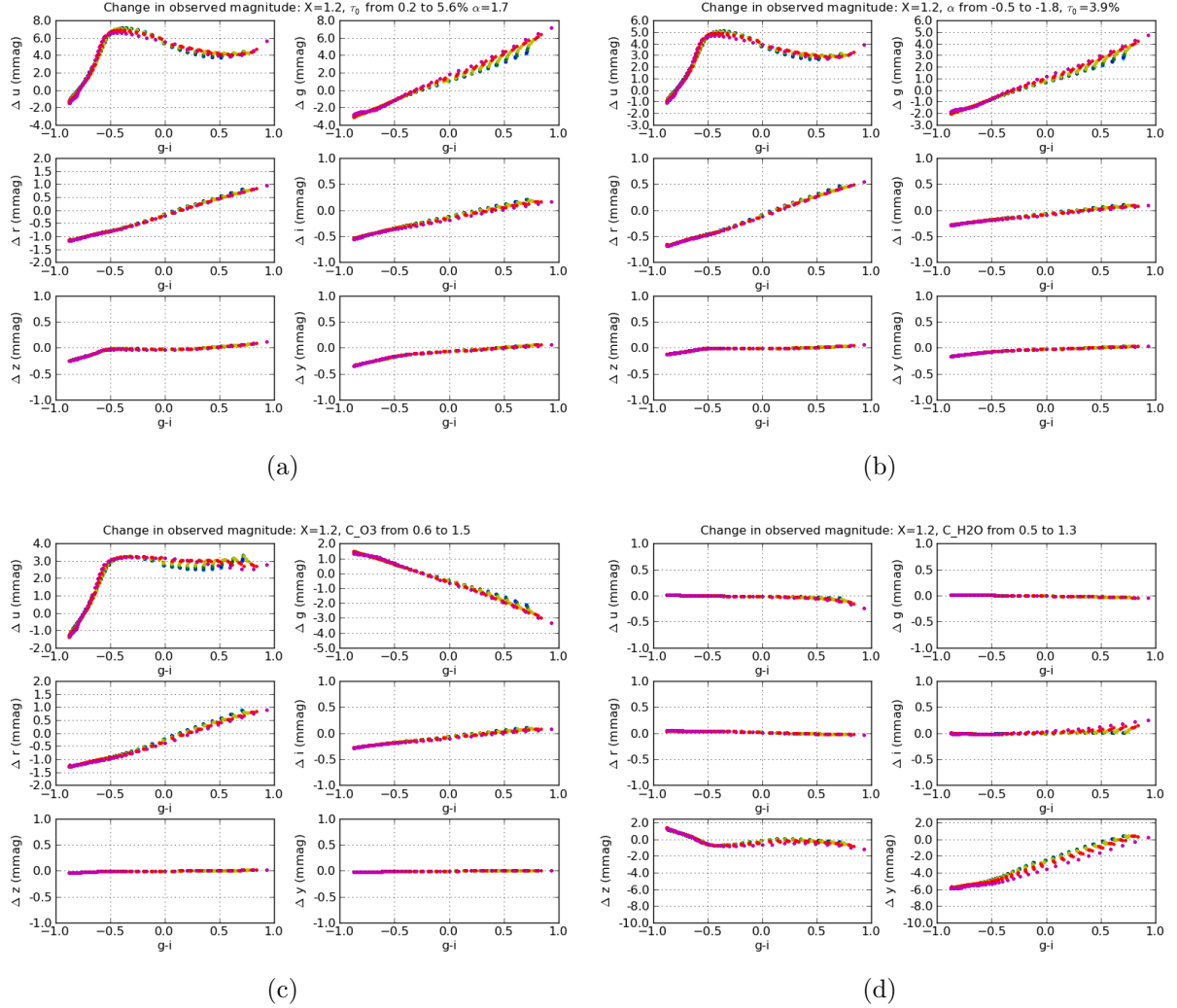
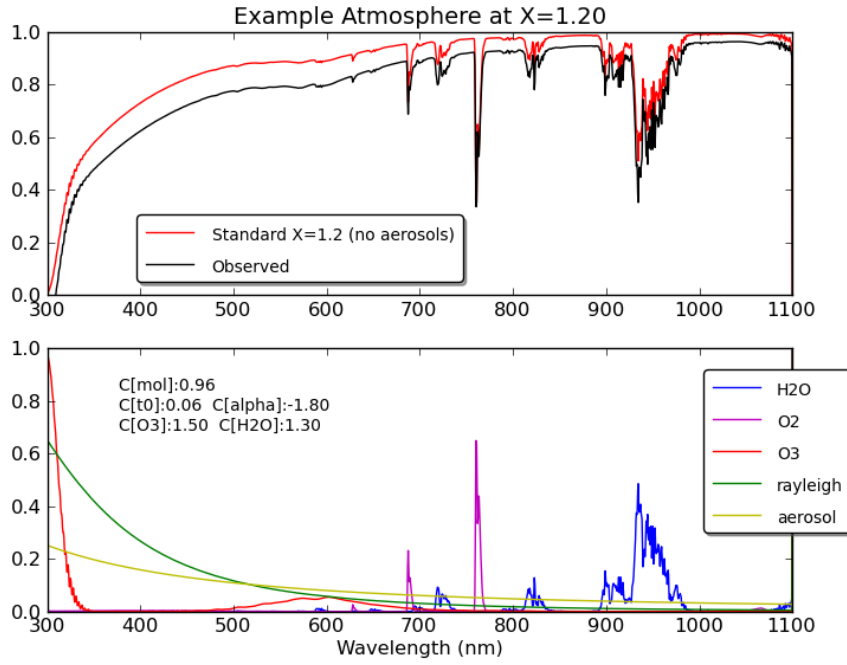
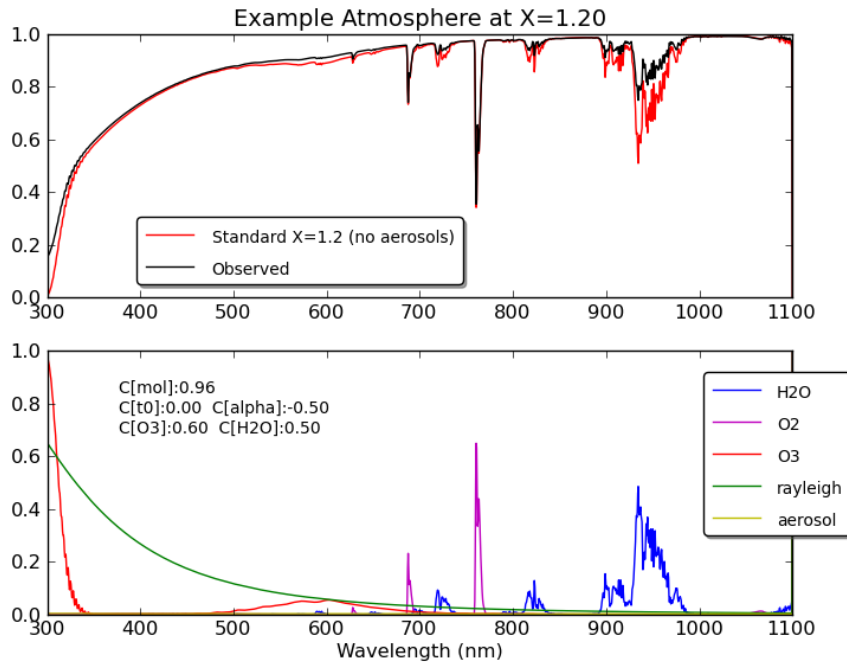


Fig. 14.—: **Changes in observed magnitudes due to variations of each individual absorption component.** Each atmospheric transmission curve (at $X=1.2$) was combined with the set of main sequence Kurucz curves to determine the resulting changes in observed magnitudes, as in Figure 10. 14a and 14b show the effects of varying aerosol absorption in τ_0 and α respectively, 14c shows the effect of varying O_3 absorption. These effects are concentrated in u and g bands, with a negligible effect in izy . 14d shows the effect of varying the H_2O absorption, which is strongest in y , with some effect in z and no effect in $ugri$.



(a)



(b)

Fig. 15.—: ‘Extreme’ atmospheres generated from MODTRAN profiles and extremes of atmospheric coefficients. Using the extremes of C_{H_2O} , C_{O_3} , and τ_0 and α from Burke et al. (2010), two test atmospheres with $X = 1.2$ were created using Equation 22.

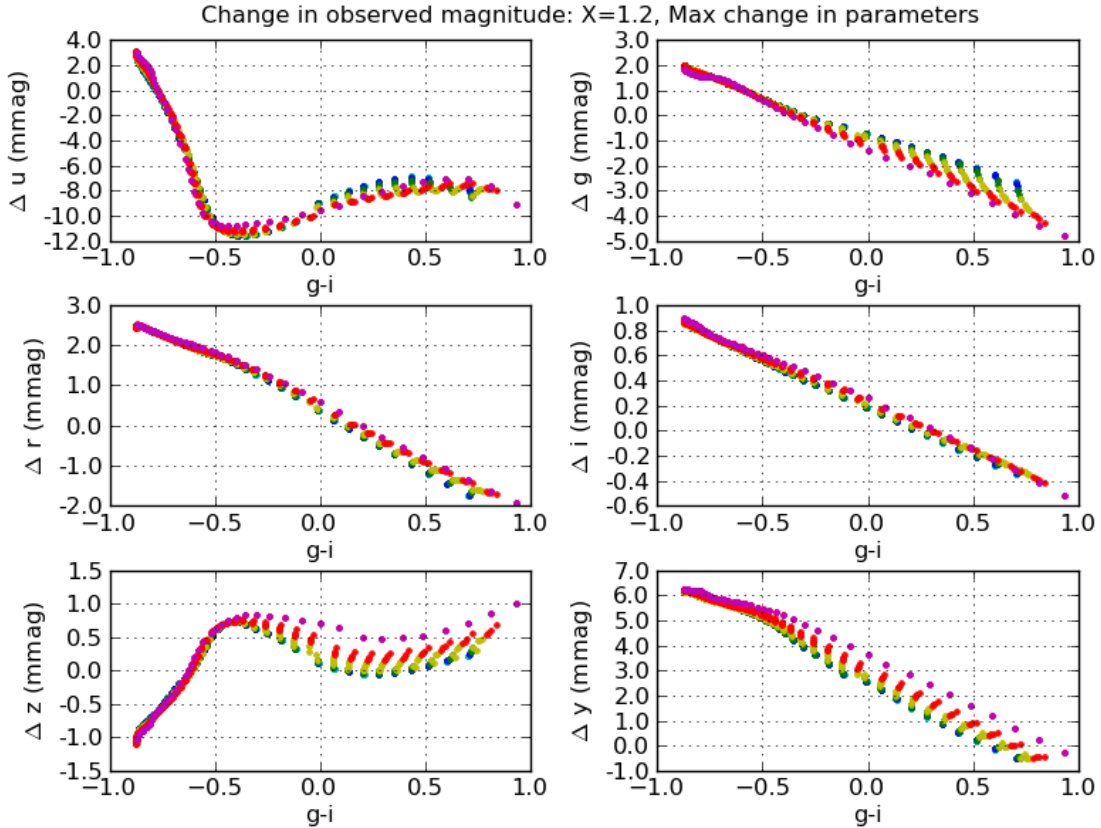


Fig. 16.—: **Changes in observed magnitudes due to ‘extreme’ variations of atmospheric transmission.** Two atmospheric transmission curves were created using Equation 22 and the widest variations of atmospheric extinction coefficients from Burke et al. (2010). The wavelength profile of these atmospheres is shown in Figure 15. These atmospheric transmission curves were combined with the baseline LSST hardware transmission curves, and used to generate magnitudes for 850 Kurucz models with temperatures between 5000 K and 35000 K and metallicities between -5.0 and 1.0 (solar). The differences in observed magnitudes between the two extremes of the atmospheric transmission in each filter are shown above.

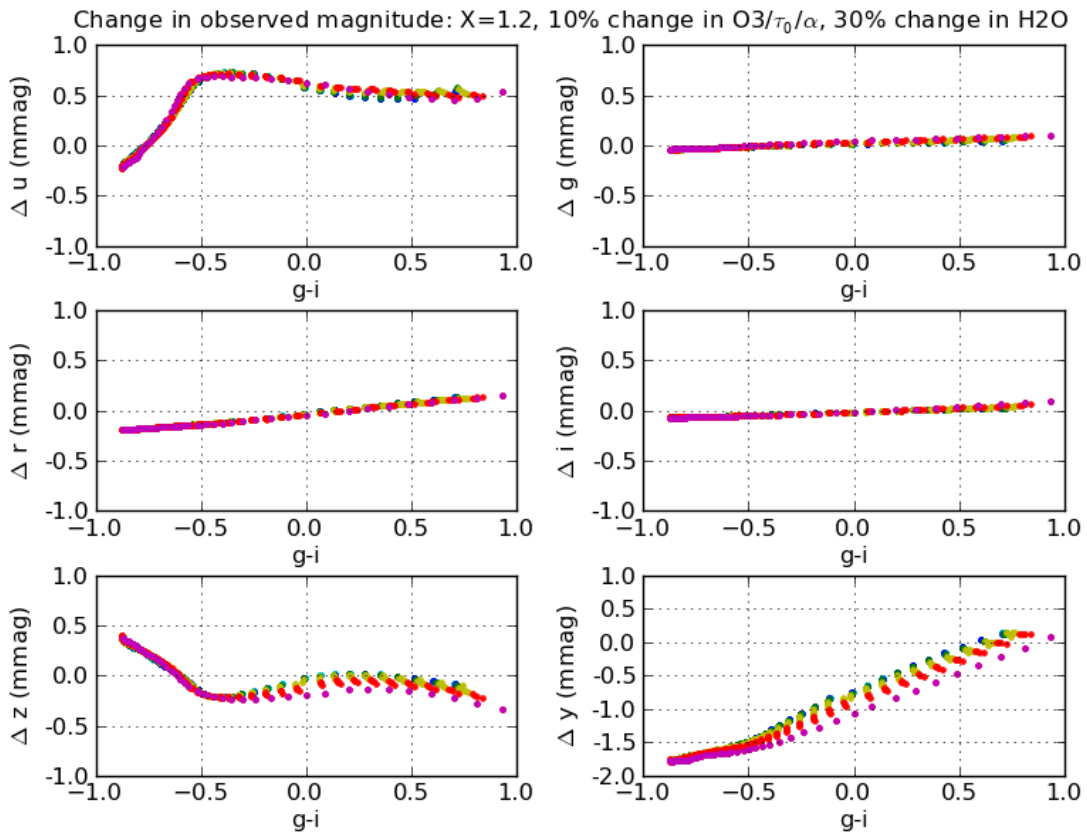


Fig. 17.—: Changes in observed magnitudes due to 10% variations of atmospheric transmission in O_3 and aerosol, with 30% variation of H_2O . This is similar to Figure 16, except C_{O_3} , τ_0 and α were only varied by 10% of the total range of values measured in Burke et al. (2010), and C_{H_2O} was varied by 30% of the total range.

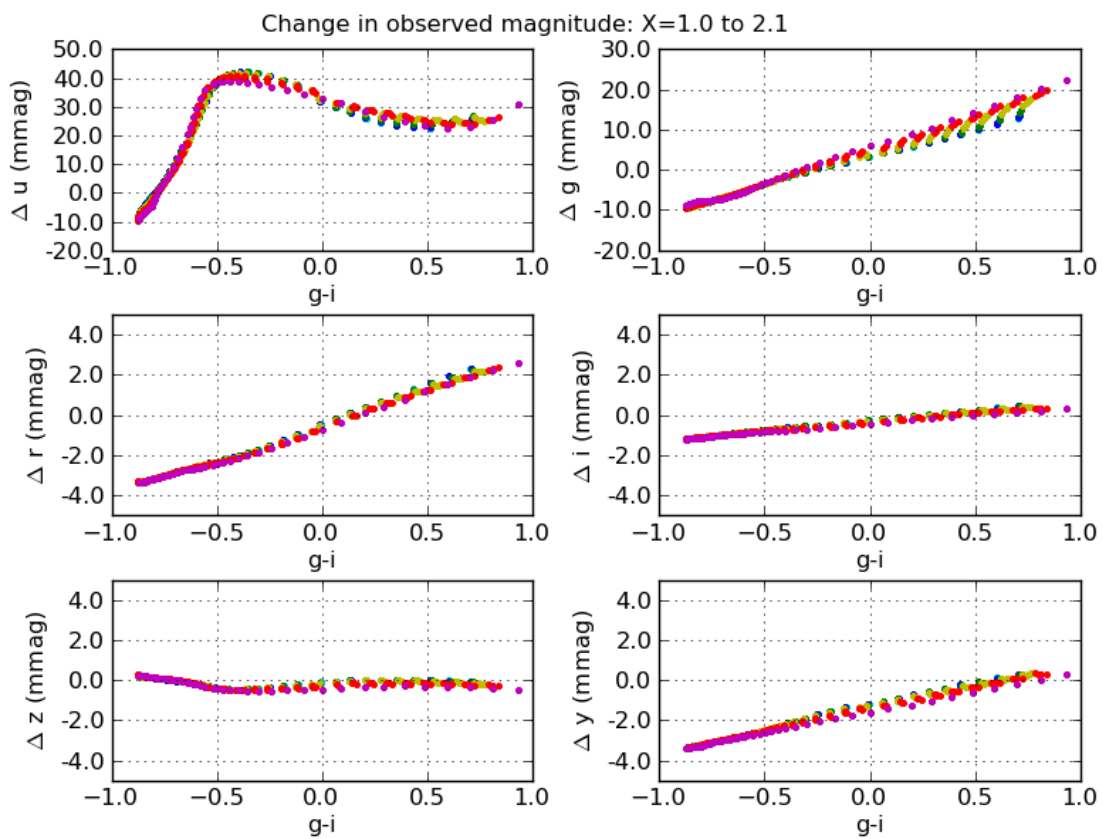


Fig. 18.—: Changes in observed magnitudes due to changes in airmass from $X = 1.0$ to $X = 2.1$, for a typical atmospheric transmission response curve.

